Field Ionization Processes of Highly Excited Rydberg States under a Rotating Electric Field

By

Satoru Yamada

Department of Physics, Kyoto University
Kyoto 606-8503, Japan

Abstract

Ionization property of highly excited Rydberg states of rubidium 85 under a rotating electric field has been investigated experimentally and theoretically. In the experiment, manifold states whose principal quantum number $112 \leq n \leq 137$ have been directly populated by a two-step laser excitation and ionized by a pulsed electric field. The pulsed electric field has been reversed through zero field and increased to ionize the Rydberg atoms. We have applied an additional static field perpendicular to the pulsed field to rotate the total electric field vector around zero field. Applying the perpendicular field, we have observed the increase of the fraction of the tunneling ionization process and the broadening of the width of its ionization peak in the ionization spectra. The n and slew rate dependence of the fraction of the tunneling ionization has also been measured. The fraction is almost flat with n ranging from 112 to 137 and decreases slightly with the increasing slew rate of the pulsed electric field.

In the theoretical simulations, we have performed two calculations of (1) transition probability between states with different magnetic quantum number m_ℓ during the electric field rotation and (2) time evolution of the states with each m_ℓ on the Stark map under the ramped field after the field rotation. These two calculations have been combined to obtain the fraction of the tunneling ionization, which has been compared with the experimental results in the present study. The theoretical results are in good agreement with the experimental ones, which demonstrates the redistribution of m_ℓ and the position in the manifold by the field rotation.

From the viewpoint of application, the increase of the tunneling process by the field rotation gives the improvement of the efficiency of selective field ionization. In the present work, we have found that the

fraction of the tunneling ionization can be increased to over 0.9 by the field rotation.

Contents

1   Introduction

Rydberg atoms are atoms with valence electrons whose principal quantum number n is very large. The studies of their property have achieved profound progress as laser techniques have been advanced. Tunable dye lasers enable us to study highly excited Rydberg atoms with n of a hundred and above.

Rydberg atoms have large transition dipole moments proportional to n^2. This means Rydberg states have large couplings to photons. In addition to that, an energy interval between adjacent states decreases with n^{-3} and reaches microwave region (2.5GHz between $111s$ and $111p$ states of ^{85}Rb). Therefore, Rydberg states have been studied as an excellent single-microwave-photon detector for dark matter axion search [1]. In the experiment, a dark matter axion is converted to a photon under the strong magnetic field of 7T in the cavity cooled to near 10mK. Rydberg atoms excited to ns state are introduced to the cavity whose resonant frequency is tuned to the transition frequency between ns and np states. The Rydberg atoms in the cavity then absorb the microwave photon converted from the axion and are excited to the upper np state. When the atom of the np state separated from the ns state is detected, it is the evidence of the axion.

In the applications of Rydberg atoms such as the microwave detection described above, selective field ionization (SFI) of atoms is the essence of the method. When an electric field is applied to the Rydberg atom, its Coulomb potential that traps the valence electron is tilted and the electron can escape over the potential barrier. Since the threshold of ionization field varies with the energy of the Rydberg state, it is possible to distinguish each state from the other states by measuring their ionization threshold fields.

Alkali Rydberg states have two processes of the field ionization [2]. One is the tunneling process: as an external electric field becomes stronger, a valence electron of a Rydberg atom escapes from the Coulomb potential barrier by tunneling. The other is the autoionization-like process, where the ionization occurs due to the transition to continuum states with higher n. The tunneling process occurs in both hydrogenic and nonhydrogenic atoms, but the autoionization-like process only occurs in nonhydrogenic atoms because the states of nonhydrogenic atoms have coupling to other n states through their large ionic core.

In the case of low-n, it is possible to distinguish the ionization peaks of the two states with $\Delta n = 1$ in the autoionization-like process. As n becomes large, however, the difference between their ionization threshold becomes too small to be resolved. For example, for $n = 112$ the difference is only about 0.1V/cm. On the other hand, the tunneling process has an advantageous

property for the selective field ionization that the ionization threshold varies largely even in the same n states [3]. At $n = 112$, the difference of the ionization field between the uppermost energy level (the bluest state) and the lowermost energy level (the reddest state) in the manifold is about 5V/cm. It is sufficient to distinguish the two levels.

Using the tunneling ionization process, the selective field ionization of $111s$ and $111p$ states of ^{85}Rb for the microwave detection has been achieved [4]. In their method, only the tunneling ionization process contributes to the selective field ionization. Therefore, if one achieves the enhancement of the fraction of the tunneling process, it improves the efficiency of the selective field ionization. This is the motivation of the present study from the viewpoint of the application.

Which of the two processes does occur depends on the coupling strength between states of different n and a slew rate of the applied electric field. When the coupling is large, the transition to continuum states instantly occurs at the classical ionization limit. The strength of the couplings depends on the principal quantum number n and the magnetic quantum number m_ℓ.

Rydberg states are usually prepared from the ground state by the laser excitation. Due to the selection rule, the final Rydberg state is allowed to have only $|m_\ell|$ close to zero. In alkali atoms, the autoionization-like process dominates in such a low-m_ℓ state, because the coupling strength between different n states is large, as will be described in Sec. 2.

Under the electric field, if the direction of the applied field does not change, m_ℓ along the field direction is a good quantum number and conserved. However, when the field rotates and changes its direction, the cylindrical symmetry is broken and the change of m_ℓ can occur. The same things can be said for the magnetic field. The perpendicular component of electric and magnetic fields to the quantization axis can cause the m_ℓ-changing transition.

In the present study, we focused on the effect of a rotating electric field, which may cause the $|m_\ell|$-changing transition. The transition will improve the selectivity in the field ionization, because it increases the fraction of larger m_ℓ states, which are ionized through the tunneling process. The applied rotating electric field in the present experiment consists of the sum of a pulsed electric field for ionization and a small static field perpendicular to the pulsed field. The pulsed field is reversed from several tens of mV/cm to about 6V/cm through zero field. While the values of the pulsed field are comparable with that of the perpendicular field, the total electric field vector rotates to the nearly opposite direction. We have called it the rotating field regime. After the rotating field regime, the pulsed electric field becomes the dominant component of the total electric field vector with rapid increase

to about 6V/cm. Here the total electric field vector does not change its direction largely. We have called it the dominant pulsed field regime. We have measured the ionization spectra with various conditions of the electric field rotation, changing the amount of the perpendicular field.

The theoretical study has also been done in the present work. To calculate the time evolution of the Rydberg states under the experimental condition described above, we have divided the simulation into two parts; the calculation in the rotating field regime and that in the dominant pulsed field regime. In the rotating field regime, m_ℓ-changing probability has been calculated but transitions to other n states are not considered because the electric field is small compared to the field at which the adjacent n manifold states begin to cross. On the other hand, in the dominant pulsed field regime, m_ℓ-changing transition has not been taken into account because we have assumed m_ℓ is nearly a good quantum number. This assumption is reasonable because the pulsed electric field is dominant and the direction of the total field vector does not change largely. In the dominant pulsed field regime, we have calculated the evolution of the states with n-changing transitions through avoided crossings of different n states.

In the rotating field regime, we have calculated the time evolution of the population of the m_ℓ states under rotating electric and static magnetic fields whose value is about the value of the geomagnetic field. We have used the scheme developed by Kazansky and Ostrovsky [5]. The time evolution of the states is like the spin motion under a magnetic field, but the effective magnetic field in this case is actually the sum of the electric and magnetic fields and the spin is actually the sum of the angular momentum and the Runge-Lenz vector. In the present study, the effect of the spin-orbit interaction and quantum defects of alkali atoms have been neglected, which should be included in a more precise calculation.

After we have obtained the m_ℓ distribution under the field rotation by the calculation above, we need to calculate the time evolution of the Rydberg states in the dominant pulsed field regime. It is aimed at obtaining the fraction of the tunneling processes in each m_ℓ. We have solved the Schrödinger equation with the Hamiltonian that contains quantum defect of ^{85}Rb and an external electric field induced term in addition to the Coulomb field term. The ℓs-coupling and Zeeman shift terms have been neglected because they are negligibly small compared to the electric field induced term. The states with the principal quantum number in the range from $n-5$ to $n+5$ are included as basis, whose total number is over 1000 in the present work with n greater than 112. In the present work, we have calculated the population distributions up to 800mV/cm in n=112 and extrapolated it to the tunneling

ionization field to obtain the fraction of the tunneling process. Combining the calculated results in the two regimes, we have obtained occurrence probabilities of the autoionization-like and tunneling processes under the rotating field theoretically.

In the present calculation in the dominant pulsed field regime, the numerically computing program was originally developed by Kishimoto [6]. However, the previous work was aimed to calculate the small region including several avoided crossings, where the number of basis is a few tens. We have extended it over 1000 and changed the basis of the Hamiltonian matrix from the eigenstates under the electric field to the spherical basis for saving the calculation time, which is needed in doing calculations with such a large number of states. In the present work, we have calculated the coherent time evolution where we have taken the phase of the wavefunction into account. Førre and Hansen [7] also did the coherent calculation of a lithium Rydberg state of relatively lower n of 25.

The experimental procedure is here described briefly as follows. We used a thermal atomic beam of ^{85}Rb. The beam was introduced to the region that was surrounded by four electrodes. In the region, the manifold states with n ranging from 112 to 137 were directly populated by a two-step laser excitation scheme. Two of the electrodes were for applying a pulsed electric field to ionize the atoms, and the other two were for applying a static field perpendicular to the ionization field. Electrons from ionized atoms were collected by an electron multiplier. Amplified signals are fed to a discriminator and their timing information was recorded through a time digitizer. The timing information was transformed to that of the ionization field by using the profile of the pulse shape, which gave the ionization spectra of the Rydberg states.

The effect of the reverse of the pulsed electric field through zero field was reported in the work of Tada et $al.$ [4] in 2002. They showed the increase of the tunneling ionization fraction under the field reversal. The mechanism of the phenomenon has been investigated in the present work. Other field reversal experiments were performed by Higgs et $al.$ [8] using helium p states with n around 41 and by Rolfes et $al.$ [9] using sodium d states with n ranging from 30 to 38 in 1982. In these works, the field-rotation effect causing m_ℓ-changing transition was not investigated.

The m_ℓ changing experiments by applying electric and magnetic fields with atoms of relatively lower-n have been done but focused mainly on the circular state, which is the state having a maximum value of $|m_\ell| = \ell = n-1$; M.Gross and J.Liang [10] studied the motion of the angular momentum under varying electric fields and demonstrated a way to make circular atoms more

Table 2.1: Atomic units.

Quantity	1 a.u.
Mass	9.1×10^{-28}g
Charge	1.6×10^{-19}C
Energy	27.2eV
Length	0.0529nm
Electric field	5.14×10^9V/cm
Magnetic field	2.35×10^9gauss

stable. Day *et al.* [11], Mogensen *et al.* [12] and Kristensen *et al.* [13] have created circular states of lithium with n of about 25 in crossed electric and magnetic fields and Lutwak *et al.* [14] have done it for hydrogen with n of about 29. Our main aim in the present study is different from theirs in that we have investigated the effect of the field rotation on the ionization more generally.

In Sec. 2, the property of Rydberg states related to the field ionization is presented. In Sec. 3, the simulation of time evolution of the Rydberg states under the field rotation is described. In Sec. 4, the setup and procedure of the experiment is shown. In Sec. 5 the experimental and theoretical results are compared and their features are discussed, and then Sec. 6 is devoted to the conclusion.

2 Rydberg atoms and field ionization

2.1 Rydberg atoms

Rydberg atoms are atoms whose valence electrons have large principal quantum numbers. The property of alkali Rydberg atoms strongly depends on only outer valance electrons. It is approximately taken as an electron moving in the Coulomb potential when the size of the ionic core is small compared to the electron orbit radius. Hydrogen atoms or high angular momentum states are in those situations. Therefore the property of Rydberg atoms obeys simple n-scaling law. In the following, firstly, features of hydrogen Rydberg states are explained. Features of alkali Rydberg atoms are described later, but they have almost the same features except low-ℓ states. Hereafter, atomic units are used. The definitions of some units are shown in Table 2.1.

First, in the zero electric and magnetic fields, the energy of a level W

with principal quantum number n is given by the Balmer formula,

$$W = -\frac{1}{2n^2}. \tag{2.1}$$

The interval ΔW between $\Delta n = 1$ states is

$$\Delta W \simeq \frac{3}{2n^3}. \tag{2.2}$$

At n of around 100, ΔW enters a microwave range.

As n grows, the "classical" radius for a Rydberg state increases. The transition dipole matrix element d when $\Delta n \simeq 1$, which is directly connected to the coupling with a photon, is described as

$$d = e < n\ell|r|n'\ell' > \propto n^2, \tag{2.3}$$

where ℓ is an orbital angular momentum.

Above description of Rydberg states can be applied to only the hydrogen or hydrogen-like atoms, which have negligible size of ionic core. In an alkali Rydberg atom, however, the ionic core has the finite size because it is made up of a nucleus and electrons other than a valence electron. When its angular momentum is low, the core affects its wavefunction. In the hydrogen, states of the same n are all degenerated, but in alkali atoms low-ℓ states such as s, p, d usually have different energy from that of other high-ℓ states.

The wavefunction of an alkali atom outside ionic core can be obtained using quantum defect theory. The effect of ionic core is "pulling" the wavefunction of hydrogen atoms to the origin of the Coulomb potential as shown in Fig. 2.1. To obtain energy of alkali Rydberg atoms, one should only replace n in Eq. (2.1) by $(n - \delta_\ell)$, where δ_ℓ is called a quantum defect. It means that a $n\ell$ state with a larger quantum defect has lower energy. Energy of alkali Rydberg states W is precisely described as

$$W = -\frac{R_{alk}}{(n - \delta_{n\ell j})^2}, \tag{2.4}$$

where R_{alk} is a Rydberg constant (109736.605 cm^{-1} for ^{85}Rb). Here,

$$\delta_{n\ell j} = \delta_0 + \frac{\delta_2}{(n - \delta_0)^2} + \frac{\delta_4}{(n - \delta_0)^4} + \frac{\delta_6}{(n - \delta_0)^6} + \frac{\delta_8}{(n - \delta_0)^8} \cdots . \tag{2.5}$$

The quantum defect parameters of ^{85}Rb are shown in Table 2.2.
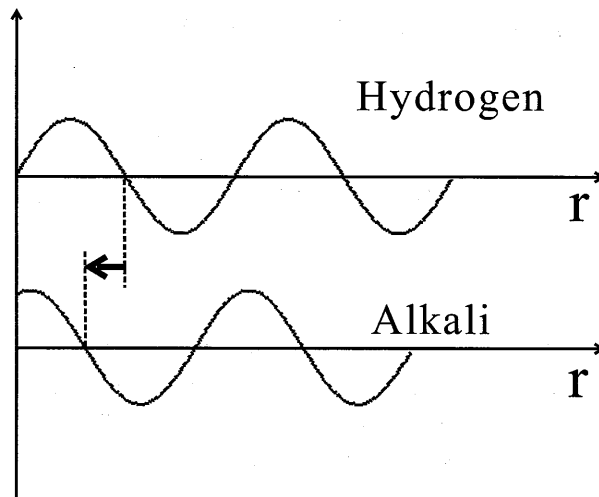
Figure 2.1: Effect of ionic core of an alkali atom on its wavefunction compared with that of hydrogen.

Table 2.2: ^{85}Rb quantum defect parameters [2].

Series	δ_0	δ_2	δ_4	δ_6	δ_8
$ns_{1/2}$	3.13109(2)	0.204(8)	-1.8		
$np_{1/2}$	2.65456(15)	0.388(60)	-7.904	116.437	-405.907
$np_{3/2}$	2.64145(20)	0.33(18)	-0.97495	14.6001	-44.7265
$nd_{3/2,5/2}$	1.347157(80)	-0.59553	-1.50517	-2.4206	19.736
$nf_{5/2,7/2}$	0.016312	-0.064007	-0.36005	3.2390	

2.2   Rydberg atoms under an electric field and their ionization processes

2.2.1   Rydberg atoms under an electric field

In this subsection, we will describe the property of Rydberg states under an electric field and their ionization property. First, we describe the property of hydrogen atom under the electric field. When the electric field F whose direction is along the z axis is applied to the Rydberg state, the Hamiltonian becomes

$$H = \frac{1}{2}p^2 - \frac{1}{r} + Fz, \tag{2.6}$$

where p is a momentum of the valence electron. In this situation, the Schrödinger equation is solved analytically by using parabolic coordinates ξ, η and ϕ;

$$\xi = r + z \tag{2.7}$$

$$\eta = r - z \tag{2.8}$$

$$\phi = \tan^{-1} y/x. \tag{2.9}$$

The Schrödinger equation is separated to two independent equations

$$\Psi(\xi, \eta) = \frac{1}{\sqrt{\xi \eta}} \Xi(\xi) H(\eta) \tag{2.10}$$

$$\frac{d^2 \Xi(\xi)}{d\xi^2} - \left(\frac{m^2 - 1}{4\xi^2} - \frac{Z_1}{\xi} - \frac{W}{2} + \frac{F}{4}\xi \right) \Xi(\xi) = 0 \tag{2.11}$$

$$\frac{d^2 H(\eta)}{d\eta^2} - \left(\frac{m^2 - 1}{4\eta^2} - \frac{Z_2}{\eta} - \frac{W}{2} - \frac{F}{4}\eta \right) H(\eta) = 0, \tag{2.12}$$

where W is the energy and Z_1 and Z_2 are the separation constants. When Eqs. (2.11) and (2.12) are solved, the wavefunction have four quantum numbers; principal quantum number n, magnetic quantum number m, and parabolic quantum numbers n_1 and n_2. They have a relation shown as

$$n = n_1 + n_2 + |m| + 1. \tag{2.13}$$

Using the wavefunction under the zero field, the first order energies $W_{nn_1n_2m}$ are,

$$W_{nn_1n_2m} = -\frac{1}{2n^2} + \frac{3}{2}Fn(n_1 - n_2). \tag{2.14}$$

The value of $n_1 - n_2$ ranges when $|m| = 0$ as $n-1, n-3, \ldots, -n+1$ and when $|m| = 1$ as $n-2, n-3, \ldots, -n+2$. The states with high $n_1 - n_2$ are called blue states, and the states with low $n_1 - n_2$ are called red states. The stark structure of hydrogen is shown by Fig. 2.2, which is called a Stark map. The electric field lift degeneracy within the same n states, which is called as a manifold.

The alkali atoms also have the features described above. However, the low-ℓ states are not degenerated even at zero field. The Hamiltonian of an alkali atom H is written as

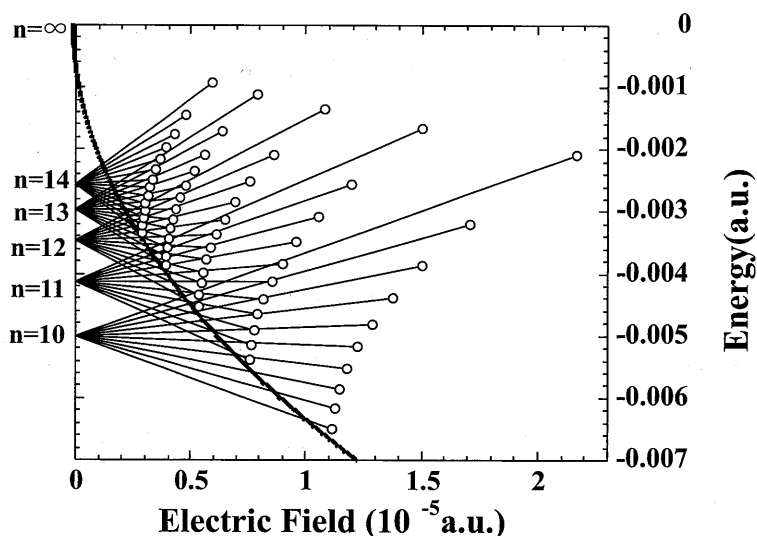$$H = \frac{1}{2}p^2 - \frac{1}{r} + Fz + V_d(r), \tag{2.15}$$

Figure 2.2: Stark structure of hydrogen of n over a range of 10 to 14. Open circles are the ionization points of the tunneling process. Solid bold line is classical ionization limit.

where $V_d(r)$ is the difference between the potential of an alkali atom and Coulomb potential. The matrix element of V_d between the same state is

$$< n\ell m|V_d(r)|n\ell m >= -\frac{\delta_\ell}{n^3}, \qquad (2.16)$$

where δ_ℓ is a quantum defect parameter of the ℓ state. Because of spherical symmetry of $V_d(r)$, it does not change ℓ and m. Between different n states, the matrix element is given by,

$$< n\ell m|V_d(r)|n'\ell m >= -\frac{\delta_\ell}{\sqrt{n^3 n'^3}}. \qquad (2.17)$$

In the representation of the parabolic basis, the matrix element is

$$< nn_1n_2m|V_d|n'n_1'n_2'm >= \sum_\ell < nn_1n_2m|n\ell m > \frac{-\delta_\ell}{\sqrt{n^3 n'^3}} < n'\ell m|n'n_1'n_2'm > .$$
$$(2.18)$$

Adding the ℓs-coupling Λ, the Hamiltonian is

$$H = \frac{1}{2}p^2 - \frac{1}{r} + Fz + V_d(r) + \Lambda. \qquad (2.19)$$
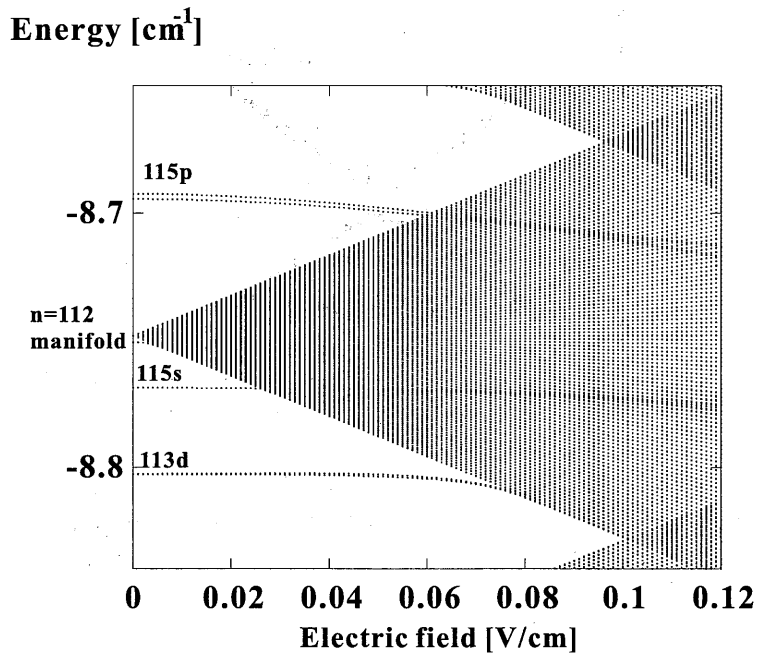
Energy [cm^{-1}]

Figure 2.3: Calculated Stark structure of ^{85}Rb with $n = 112$ and $|m_j| = 1/2$.

The diagonalization of Eq. (2.19) cannot be achieved analytically as a hydrogen atom, but it can be done numerically. We have followed the work of Kishimoto *et al.* [6] to calculate the Stark map of ^{85}Rb. In Fig. 2.3, ^{85}Rb Stark map whose energy is around $n = 110$ is shown. While manifold states are shifted almost linearly with the electric field, s, p, d and f states shift in proportion to F^2 as the field increases, because the low-ℓ states do not have a permanent electric dipole moment.

2.2.2 Avoided crossing

One of the most important features of alkali atoms for ionization is the existence of avoided crossings at crossings between different levels. In hydrogen, a state of $|nn_1n_2m >$ does not have a coupling to the other states, but in alkali atoms, as shown in Eq. (2.18), manifold states have couplings with other states due to their quantum defects, which result in avoided crossings. While a Rydberg state with n of around 100 propagates on the Stark map from near zero field to the ionization field, it crosses over a few thousand avoided crossings. As shown in Fig. 2.4, at each avoided crossing there are two paths to go through. One is the adiabatic passage(solid arrow in Fig.
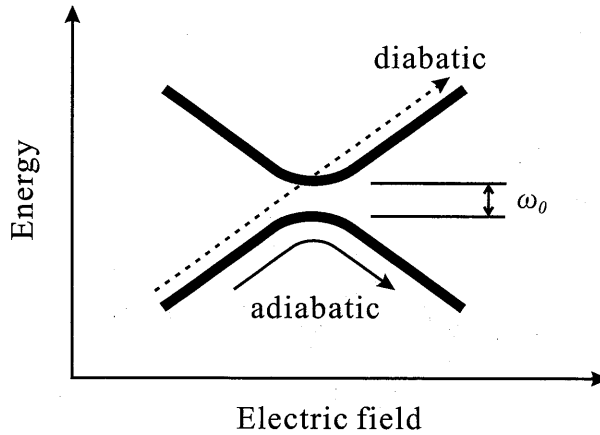
Figure 2.4: Two Stark levels with an avoided crossing of ω_0. If the field is driven through the avoided crossing in a long time compared to $1/\omega_0$, the passage is adiabatic(solid arrow), while if it is driven rapidly, the passage is diabatic(dashed arrow).

2.4) and the other is the diabatic passage(dashed arrow in Fig. 2.4). In the crossing of two levels, the probability P of passing through the crossing diabatically is given by the Landau-Zener model [15],

$$P = \exp\left(-2\pi \frac{|<V_d>|^2}{\hbar \frac{d\Delta W}{dF} \cdot \frac{dF}{dt}}\right). \tag{2.20}$$

where $<V_d>$ is a matrix element of $V_d(r)$ between the two states, ΔW is the difference of the energy between the two states, F is an electric field and $\frac{dF}{dt}$ is a slew rate of the electric field. The probability P increases with increasing slew rate of the electric field, but decreases with the coupling between the states. The coupling $|<V_d>|$ increases with increasing quantum defect, but decreases with increasing principal quantum number from Eq. (2.17).

2.2.3 Tunneling and autoionization-like processes

To describe field ionization of Rydberg atoms, we will begin from a classical picture first. In Fig. 2.5(a), no field is applied and an electron is confined in the Coulomb potential. In Fig. 2.5(b), an external field is applied and the electron can escape from the tilted Coulomb potential. The relation between the threshold field F and the electron energy W is

$$F = \frac{W^2}{4}. \tag{2.21}$$
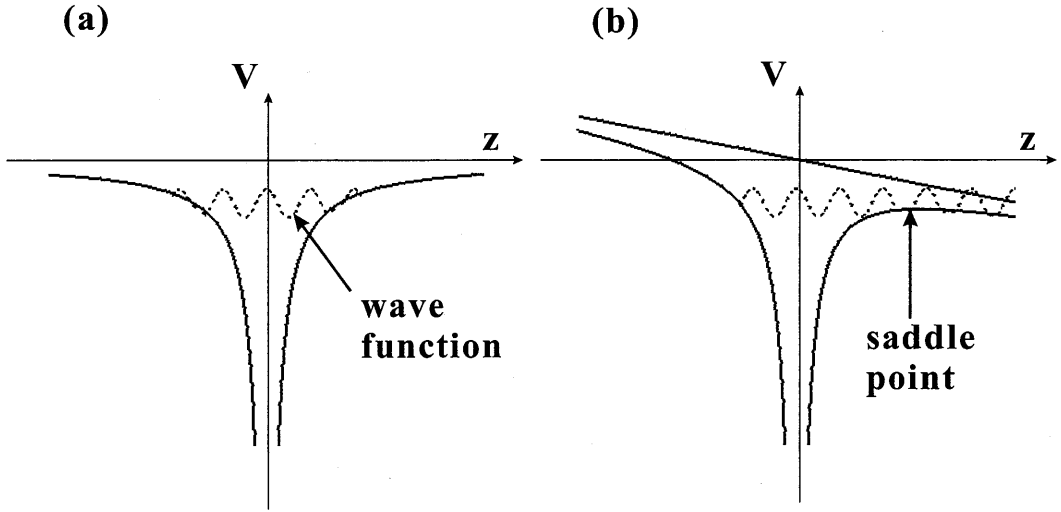
(a) **(b)**

Figure 2.5: Schematic view of the field ionization. Potential(solid curve) and wavefunction (dashed curve) (a) without and (b) with an external electric field(solid line) are shown. In Fig.(a), the wave function is confined by the Coulomb potential. In Fig.(b), by the external field, the Coulomb potential is tilted and the wavefunction is going out of the potential barrier.

It is rewritten by n as

$$F = \frac{1}{16n^4}. \qquad (2.22)$$

That is classical ionization limit as a solid curve shown in Fig. 2.2.

The classical picture above is not correct because Eq. (2.22) does not take the Stark shift and the spatial distribution of the wavefunction into account. But accidentally F in Eq. (2.22) coincides with the ionization threshold of autoionization-like process described below.

In the ionization of alkali Rydberg states, there are two different ionization processes. One is the tunneling process, and the other is the autoionization like process. Autoionization-like process occurs only on nonhydrogenic atoms, while tunneling process does both on hydrogen and nonhydrogenic atoms.

Tunneling process is the process that an electron escapes from Coulomb potential by tunneling. Its picture resembles the classical one of Fig. 2.5. However, the ionization thresholds do not obey Eq. (2.21). It shows the opposite feature; the higher states in the manifold ionize at a higher electric field. The ionization field distribution is shown in Fig. 2.2 with open circles.

On the other hand, ionization through the autoionization-like process occurs in the lower field than that of tunneling process. It occurs after the field exceeds the classical ionization limit in Eq. (2.21). When the state crosses over the classical ionization limit line as electric field increases, it begins to cross levels of higher n, which are already continuum states and have a very short life to ionize through the tunneling process. When an adiabatic transition to those continuum states occurs, the atom ionizes immediately.

2.2.4   Ionization field of the two processes

The important difference between the autoionization-like process and tunneling process is in their dependence of the ionization threshold on the energy level in the manifold. We point the energy in the manifold using a variable W_r which is defined as,

$$W_r = Z_1 - Z_2 = \frac{n_1 - n_2}{n}, \tag{2.23}$$

where Z_1 and Z_2 are the separation constants in Eq. (2.12), and n_1 and n_2 are the parabolic quantum numbers. W_r ranges from 1 to -1 when m is small. The state of $W_r = 1$ is the highest energy state in the manifold and that of $W_r = -1$ is the lowest energy state in the manifold. The $Z_1 - Z_2(= W_r)$ dependence of the ionization threshold is shown in Fig. 2.6. In the figure, solid circles are ionization thresholds of tunneling process, and open circles are those of autoionization-like process. It is obvious that the ionization thresholds of tunneling process largely varies with W_r, while the thresholds of autoionization-like process make a small change with W_r.

3   Theory of time evolution of Rydberg states

We have developed theoretical studies of the time evolution of the highly excited Rydberg manifold states of ^{85}Rb with n ranging from 112 to 137 under the rotating field. The main purpose of the calculation is to obtain the fraction of the tunneling ionization process and its dependence on the physical parameters. The rotating field considered in the present study consists of the sum of a pulsed field and a static field as shown in Fig. 3.1. The pulsed field has been reversed from several tens of mV/cm to about 6V/cm through zero field. The static field up to a few tens of mV/cm is perpendicular to the pulsed field.

We have divided the simulations into calculations in two regimes. One regime is the rotating field regime when the magnitude of the pulsed field and the perpendicular field are comparable. In the regime, the electric field
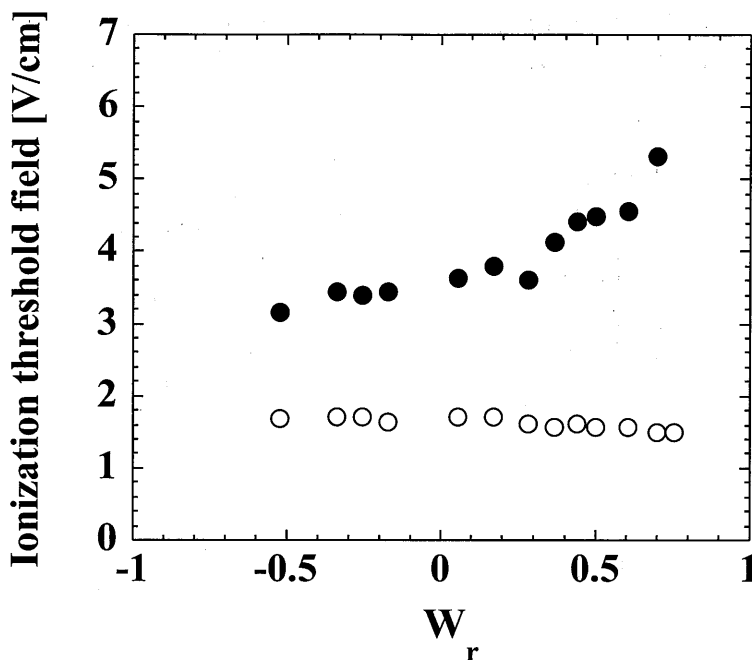
Figure 2.6: Ionization electric fields of ^{85}Rb with $n = 120$ manifold as a function of the excited position W_r. Solid circles are the ionization thresholds of the tunneling process and open circles are that of autoionization-like process. The ionization thresholds of tunneling process largely change with W_r, while the thresholds of autoionization-like process make a small change with W_r. The data are cited from [6].

rotates and m_ℓ-changing transition has occurred. However, the electric field is smaller enough than the crossing field between the adjacent n manifold states. Therefore, there are no n-changing transitions. The other regime is the dominant pulsed field regime when the pulsed electric field becomes dominant in the total electric field vector after the rotating field regime. In the dominant pulsed field regime, m_ℓ-changing transition has been ignored, assuming that m_ℓ is nearly a good quantum number by the approximate cylindrical symmetry around the pulsed field. Instead, transitions to different n states occur through avoided crossings between different n states.

In Sec. 3.1, the time evolution in the rotating field regime is calculated using the scheme developed by Kazansky and Ostrovsky [5]. We have obtained the population of magnetic quantum number m_ℓ and the position in the manifold W_r here. In Sec. 3.2, the time evolution of the states in each

(a) initial electric field vector
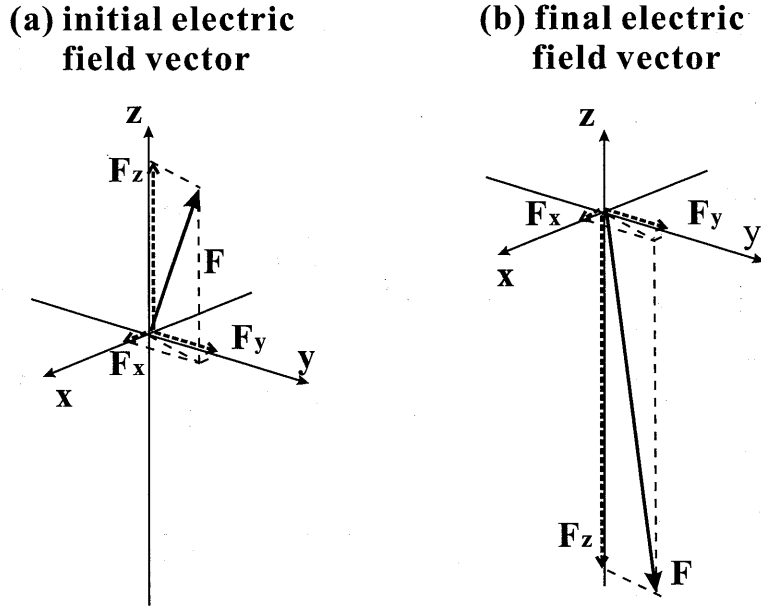
(b) final electric field vector

Figure 3.1: Schematic view of the field rotation; (a) Initial electric field vector, where Rydberg atoms are prepared and (b) Final electric field vector, where Rydberg atoms are ionized. Here, F_x and F_y are static and F_z changes its direction during the field rotation.

$|m_\ell|$ in the dominant pulsed field regime is described. We have obtained the fraction of the tunneling process in each m_ℓ state. The combination of the above two calculations gives the overall tunneling process fraction under the rotating field, which has been compared with the experimental results in Sec. 5.

3.1   Time evolution under field rotation

3.1.1   Theory of time evolution under electric and magnetic fields

In the present subsection, we describe the time evolution of a hydrogen atom under electric and magnetic fields with an arbitrary time dependence. First, the Hamiltonian of the valence electron of the hydrogen atom under an electric field $\mathbf{F}$ and a magnetic field $\mathbf{B}$ is given by

$$H = H_0 + \mathbf{F}(t)\mathbf{r} + \frac{1}{2}\mathbf{B}(t)\boldsymbol{\ell}, \tag{3.1}$$

where H_0 is the unperturbed atomic Hamiltonian, $\mathbf{r}$ is the electron vector relative to the atomic nucleus and $\boldsymbol{\ell}$ is the orbital angular momentum.

Next, Runge-Lenz vector $\mathbf{A}$ [16] is introduced. It is defined by

$$\mathbf{A} = (-2H_0)^{-1/2} \left(\frac{1}{2}(\mathbf{p} \times \boldsymbol{\ell} - \boldsymbol{\ell} \times \mathbf{p}) - \frac{\mathbf{r}}{r} \right), \qquad (3.2)$$

where $\mathbf{p}$ is a momentum vector. In parabolic coordinates, the operator A_z is diagonal, as shown,

$$< n_1 n_2 m | A_z | n_1 n_2 m > = n_2 - n_1, \qquad (3.3)$$

while z is also diagonal,

$$< n_1 n_2 m | z | n_1 n_2 m > = \frac{3}{2} n(n_2 - n_1). \qquad (3.4)$$

Therefore in this subspace, $\mathbf{r}$ can be replaced by $\mathbf{A}$ described as,

$$\mathbf{r} = -\frac{3}{2} n \mathbf{A}. \qquad (3.5)$$

The Hamiltonian after this replacement becomes

$$H = H_0 - \frac{3}{2} n \mathbf{F}(t) \mathbf{A} + \frac{1}{2} \mathbf{B}(t) \boldsymbol{\ell}, \qquad (3.6)$$

and it is further transformed to

$$H = H_0 + \boldsymbol{\omega}_1(t) \mathbf{I}_1 + \boldsymbol{\omega}_2(t) \mathbf{I}_2 \qquad (3.7)$$

$$\mathbf{I}_1 = \frac{1}{2}(\boldsymbol{\ell} + \mathbf{A}), \mathbf{I}_2 = \frac{1}{2}(\boldsymbol{\ell} - \mathbf{A}) \qquad (3.8)$$

$$\boldsymbol{\omega}_1(t) = \frac{3}{2} n \mathbf{F}(t) + \frac{1}{2} \mathbf{B}(t) \qquad (3.9)$$

$$\boldsymbol{\omega}_2(t) = -\frac{3}{2} n \mathbf{F}(t) + \frac{1}{2} \mathbf{B}(t). \qquad (3.10)$$

The vector operators $\mathbf{I}_1$ and $\mathbf{I}_2$ obey the commutation rule of angular momentum operators as established by Pauli [17]. The two operators are independent with each other and have equal magnitudes: $\mathbf{I}_1^2 = \mathbf{I}_2^2 = j(j + 1)$ with $j = \frac{1}{2}(n - 1)$. These equations show that the problem now comes into the motion of spin $\mathbf{I}_1$ and $\mathbf{I}_2$ under the fields $\boldsymbol{\omega}_1$ and $\boldsymbol{\omega}_2$. From [18] the time evolution of $\mathbf{I}_1$ and $\mathbf{I}_2$ is reduced to the $j = 1/2$ problem. The Schrödinger equations of the $j = 1/2$ spin motion are

$$i\frac{\partial \chi_1^{(k)}}{\partial t} = \frac{1}{2}\omega_{kz}(t)\chi_1^{(k)} + \frac{1}{2}(\omega_{kx} - i\omega_{ky})\chi_2^{(k)} \qquad (3.11)$$

$$i\frac{\partial \chi_2^{(k)}}{\partial t} = -\frac{1}{2}\omega_{kz}(t)\chi_2^{(k)} + \frac{1}{2}(\omega_{kx} + i\omega_{ky})\chi_1^{(k)} \qquad (3.12)$$

By solving Eqs. (3.11) and (3.12), time-propagation matrices $U^{(k)}(t,t')$ defined as $\chi_i^{(k)}(t) = U_{ij}^{(k)}(t,t')\chi_j^{(k)}(t')$ are obtained. They are parameterized with Euler angles $\alpha^{(k)}$, $\beta^{(k)}$ and $\gamma^{(k)}$ as follows:

$$U_{11}^{(k)}(t,t') = U_{22}^{(k)}(t,t')^* = \cos\frac{1}{2}\beta^{(k)} \exp\left[-i\frac{1}{2}(\alpha^{(k)} + \gamma^{(k)})\right] \quad (3.13)$$

$$U_{12}^{(k)}(t,t') = -U_{21}^{(k)}(t,t')^* = \sin\frac{1}{2}\beta^{(k)} \exp\left[i\frac{1}{2}(\alpha^{(k)} - \gamma^{(k)})\right] \quad (3.14)$$

After obtaining the Euler angle, we can solve the original problem with large $j(= \frac{1}{2}(n-1))$. We use the basis set $|i_1 i_2 >$, where i_1 and i_2 are the eigenvalues for the projections of the $\mathbf{I}_1$ and $\mathbf{I}_2$ to some fixed axes. The time propagation matrix $U^{\text{Ryd}}(t,t')$ is

$$< i_1 i_2 | U^{\text{Ryd}}(t,t') | i_1' i_2' > = D_{i_1 i_1'}^j(\alpha^{(1)}, \beta^{(1)}, \gamma^{(1)}) D_{i_2 i_2'}^j(\alpha^{(2)}, \beta^{(2)}, \gamma^{(2)}), \quad (3.15)$$

where $D_{mm'}^j(\alpha, \beta, \gamma)$ is the Wigner function [18].

When the ionization of Rydberg atoms occurs in the present experiment, the electric field is large enough that the electric field term is dominant in Eqs. (3.9) and (3.10). In this situation, we can assume in good approximation the parabolic quantum numbers m and $n_1 - n_2$ are good quantum numbers with the quantization axis along the electric field vector. Taking i_1 and i_2 as the projection of I_1 and I_2 to the electric field direction, they are related to m and $n_1 - n_2$:

$$m = i_1 - i_2 \qquad (3.16)$$

$$n_1 - n_2 = i_1 + i_2. \qquad (3.17)$$

Under the initial electric field under which the Rydberg states are excited to, we describe the initial state as $|i_1'' = \frac{m'' + (n_1'' - n_2'')}{2}, i_2'' = \frac{m'' - (n_1'' - n_2'')}{2}; \text{init} >$. If the quantization axis does not coincide with that of the final state, we need to transform the initial state to a linear combination of the eigenfunctions $|i_1' i_2' >$ of the final Hamiltonian:

$$|i_1'' i_2''; \text{init} > = \sum_{i_1' i_2'} D_{i_1'' i_1'}^j(\alpha_0, \beta_0, 0) D_{i_2'' i_2'}^j(\alpha_0, \beta_0, 0) |i_1' i_2' >, \qquad (3.18)$$

where α_0 and β_0 are Euler angles between the initial and final quantization axes. The population P_{m,n_1-n_2} of the final state with m and $n_1 - n_2$ is obtained as

$$P_{m=i_1+i_2,n_1-n_2=i_1-i_2} = | \sum_{i_1',i_2'} < i_1 i_2 |U^{\text{Ryd}}(t,t')|i_1' i_2' >< i_1' i_2' |i_1'' i_2''; \text{init} > |^2.$$

(3.19)

3.1.2 Simulation of the time evolution under field rotation

We have performed the simulation of the time evolution of the Rydberg states under the field rotation, using the procedure illustrated in the previous subsection. Parameters of the simulation are set to be near the parameters used in the experiment of Rb atoms described in Sec. 5. It is noted that the simulation scheme in Sec. 3.1.1 is applied directly only to the hydrogen case. Therefore, we should recognize that the comparison with the experimental results of Rb atoms is an approximate one to some extent.

The schematic view of the field rotation in this simulation is shown in Fig. 3.1. The main component of the electric field is F_z, which starts from $+80\text{mV/cm}(n = 112)$ at the laser excitation and increases up to about -6V/cm to ionize Rydberg atoms. The components F_x and F_y are static fields, which appear as a stray field or a field applied by side electrodes in the experiment. The magnitude of $|F_x|$ and $|F_y|$ ranges from 0 to 30mV/cm. By the existence of F_x or F_y, a total field vector $\mathbf{F} = (F_x, F_y, F_z)$ rotates during F_z reverses its direction. On the other hand, if the magnitude of F_x, F_y(and magnetic field) is zero, m_ℓ of the state does not change from the initial value.

Magnetic field is also taken into account as the geomagnetic field $\mathbf{B}^{\text{geo}}$. Taking y axis as north, and x axis as east, the components of geomagnetic field near Kyoto are,

$$
\begin{aligned}
\mathbf{B}_x^{\text{geo}} &= 0.0376(\text{gauss}) \\
\mathbf{B}_y^{\text{geo}} &= 0.310(\text{gauss}) \\
\mathbf{B}_z^{\text{geo}} &= -0.353(\text{gauss})
\end{aligned}
$$

(3.20)

The initial and final states are specified with the parabolic quantum numbers m_ℓ and $n_1 - n_2$ with the quantization axis along the z axis as shown in Eq. (3.17). When $F_z z \gg F_x x$, $F_y y$ and $\frac{1}{2}\mathbf{B}\boldsymbol{\ell}$, the parabolic basis approximately coincide with the eigenstates of energy. We have applied this assumption to the final states where F_z is relatively large. At the initial state, F_z is large compared to F_x and F_y. However, in the present study the

value of F_x and F_y have been taken into account to obtain the more precise initial state especially in the large F_y region, which will be described later.

First, a typical time evolution of $\cos \beta$ in Eq. (3.14) is shown in Fig. 3.2 with $F_y = 20\text{mV/cm}$, $\mathbf{B} = \mathbf{B}^{\text{geo}}$ and slew rate$= 6\text{V/(cm}\cdot\mu\text{s})$. The angle $\beta^{(k)}$ is a relative change of the angle between spin $\mathbf{I}_k$ in Eq. (3.8) and z axis from the initial state. Fig. 3.2 shows that the value of $\cos \beta$ changes mainly when F_z crosses zero. After that zero crossing, although it is still oscillating, the average value is almost flat. We have substituted this average value in Eq. (3.15) to obtain the distribution of m_ℓ and $n_1 - n_2$ in the final state. When $\beta^{(k)} = \pi$, which is the adiabatic limit, Eq. (3.15) becomes

$$| < i_1 i_2 |U^{\text{Ryd}}(t,t')|i'_1 i'_2 > | = \delta_{i_1 - i'_1} \delta_{i_2 - i'_2}. \qquad (3.21)$$

When $\beta^{(k)} = 0$, which is the diabatic limit, Eq. (3.15) becomes

$$| < i_1 i_2 |U^{\text{Ryd}}(t,t')|i'_1 i'_2 > | = \delta_{i_1 i'_1} \delta_{i_2 i'_2}. \qquad (3.22)$$

When $F_z z \gg F_x x$, $F_y y$ and $\frac{1}{2}\mathbf{B}\boldsymbol{\ell}$, $|m_\ell|$ does not change from the initial value in both of the two limit. Therefore to cause the $|m_\ell|$ redistribution, one should take the parameters F_x or F_y in the intermediate range like in Fig. 3.2.

When $\sqrt{F_x^2 + F_y^2}$ becomes comparable to the magnitude of the initial F_z, which is about 80mV/cm for $n = 112$ in the present experiment, it should be taken into account that the direction of the initial $\mathbf{F}$ differs largely from the z axis. In this condition, the state with m_ℓ with the quantization axis in the initial $\mathbf{F}$ direction is not an eigenstate of m_ℓ with the quantization axis along z axis as shown in Eq. (3.18). It means that even at the diabatic limit the redistribution of $|m_\ell|$ occurs.

Putting together above discussion, the m_ℓ redistribution is caused by the field rotation through (1) the spin $\mathbf{I}_k$ rotation following the rotating field described in Eq. (3.15) and (2) the rotation of the quantization axes described in Eq. (3.18).

In Fig. 3.3 the m_ℓ distributions after the field rotation are shown. The initial state is set to $n = 112, m_\ell = 0$ and $W_r = 0.52(n_1 - n_2 = 57)$, with the quantization axis as the direction of the initial $\mathbf{f}$. In Fig. 3.3(a), with no magnetic field and small electric field perpendicular to z axis ($F_y = 0.1\text{mV/cm}$), almost all the population stays in $m_\ell=0$. It is the situation where the system approximately has a cylindrical symmetry around z axis and m_ℓ can be assumed a good quantum number. In the Fig. 3.3(b), there is no electric field perpendicular to z axis but the geomagnetic field exists. The magnetic field as much as 0.47gauss makes the population of m_ℓ ranging over the region of
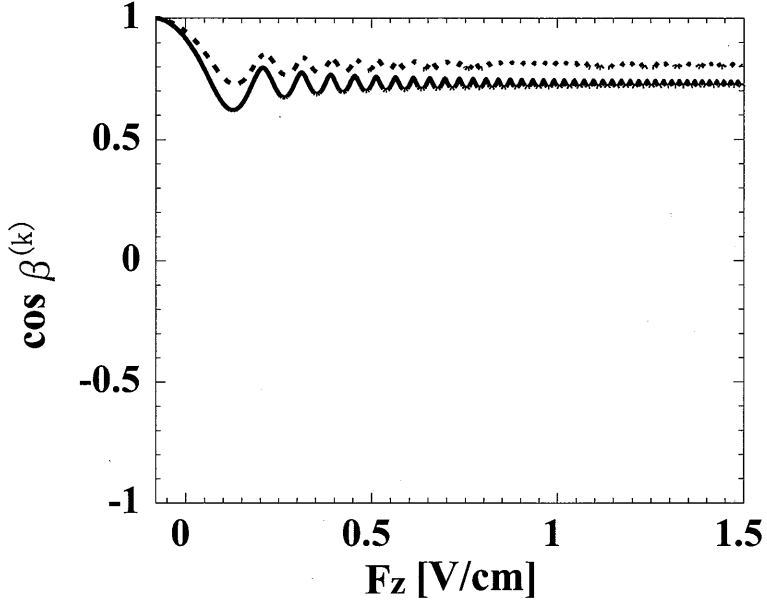
Figure 3.2: Calculated results of evolution of $\cos\beta^{(k)}$ of Eq. (3.14) as a function of F_z, which varies from -80mV/cm to 1.5V/cm. Solid line and dashed line show $\cos\beta^{(1)}$ and $\cos\beta^{(2)}$ respectively. The parameters are as follows; $n=112$, $F_y = 20$mV/cm, $\mathbf{B} = \mathbf{B}^{\text{geo}}$, slew rate= 6V/(cm·$\mu$s).

$|m_\ell| \leq 10$. With $F_y = 20$mV/cm, the population distributes more widely, as shown in Fig. 3.3(c) and the population of the $m_\ell = 0$ state decreases drastically to 1.3%.

In Fig. 3.4(a)-(c), $W_r(= \frac{n_1-n_2}{n})$ distribution under the rotating field is shown. In the figure, we have set the positive direction of the quantization axis to the direction of the final F_z, where $W_r = 1$ and -1 point highest and lowest energy levels in the manifold respectively. The figure shows that the initial state in the higher part of a manifold ($W_r = 0.52$) appears in the lower part($W_r < 0$) after the field rotation. The calculation parameters are the same as those of Fig. 3.3(a)-(c) respectively. The width of the peaks shows the similar dependence to that in Fig. 3.3. The existence of F_y or $\mathbf{B}$ makes the population range widely. It is noted that W_r distribution can be observed in an ionization spectrum. The distribution range is interpreted to a width of the tunneling ionization peak. The comparison with the experimental results is done in Sec. 5.

In Fig. 3.3 and 3.4, the results include the both effects of rotating spin $\mathbf{I}_k$
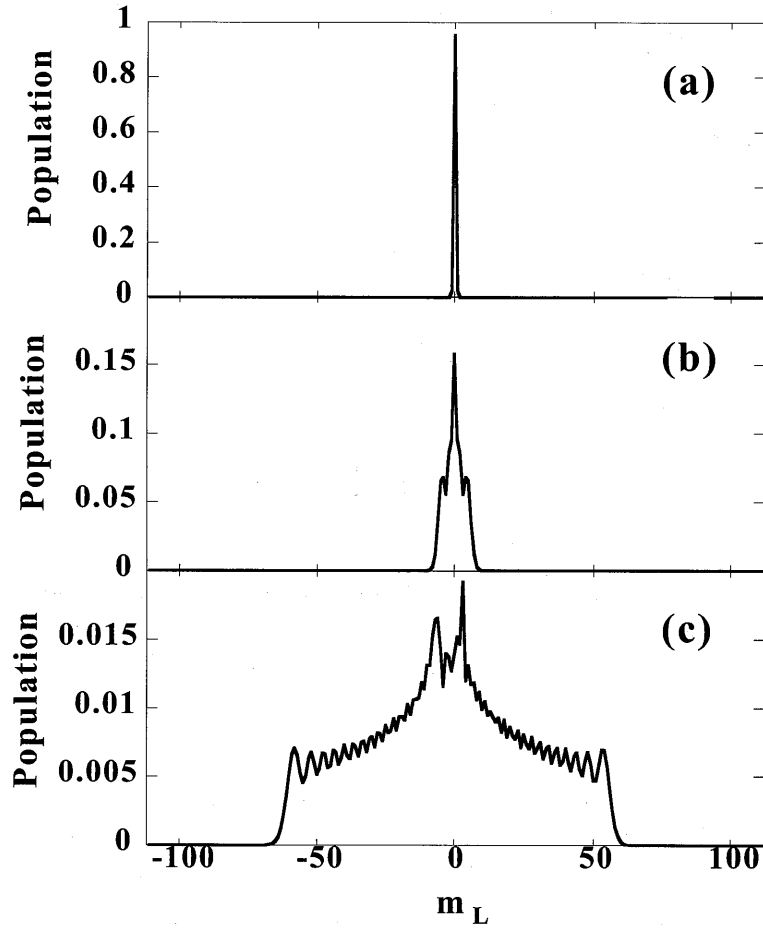
Figure 3.3: Calculated results of magnetic quantum number m_ℓ distributions after the field rotation for n=112 with (a)$F_y = 0.1$mV/cm, $\mathbf{B} = 0$gauss, slew rate= 6V/(cm·μs), (b)$F_y = 0$mV/cm, $\mathbf{B} = \mathbf{B}^{\mathrm{geo}}$, slew rate= 6V/(cm·$\mu$s), (c)$F_y = 20$mV/cm, $\mathbf{B} = \mathbf{B}^{\mathrm{geo}}$ and slew rate= 6V/(cm·μs). Initial magnetic quantum number m_ℓ is zero and $F_x = 0$mV/cm. The value of F_z varies from 80mV/cm to -6V/cm. Initial $W_r = 0.52$ with the quantization axis along the initial $\mathbf{F}$. The sum of the population over all the m_ℓ states is normalized to unity.
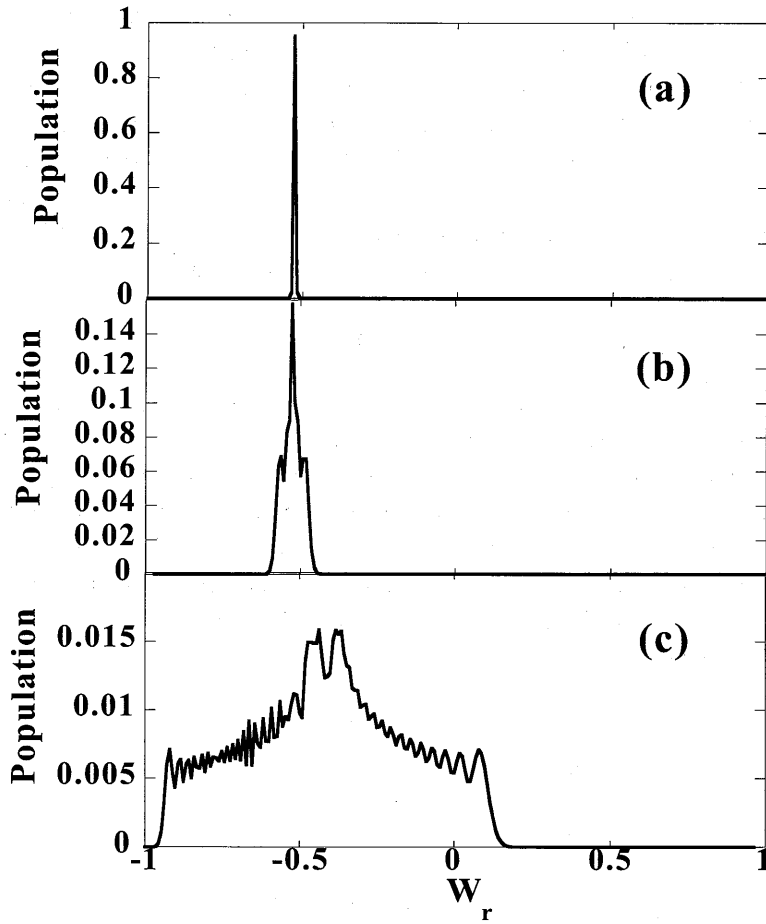
Figure 3.4: Calculated distributions of W_r for $n = 112$ after the field rotation with quantization axis along the z axis. In the field rotation, the value of F_z varies from 80mV/cm to -6V/cm. In the initial state, $W_r = 0.52$ with the quantization axis along the initial **F**. Three graphs show the results of the different conditions with (a)$F_y = 0.1$mV/cm, $B = 0$gauss, slew rate= 6V/(cm·μs), (b)$F_y = 0$mV/cm, $\mathbf{B} = \mathbf{B}^{\mathrm{geo}}$, slew rate= 6V/(cm·μs) (c)$F_y = 20$mV/cm, $\mathbf{B} = \mathbf{B}^{\mathrm{geo}}$ and slew rate= 6V/(cm·μs). Initial magnetic quantum number is $m_\ell = 0$ and $F_x = 0$mV/cm. The sum of the population over all the W_r states is normalized to unity.

and quantization axes. We have investigated the each effect in Fig. 3.5. The m_ℓ and W_r distributions are shown with the parameters: F_x, F_y and $\mathbf{B}$ are 0mV/cm, 20mV/cm and $\mathbf{B}_{\text{geo}}$, respectively, which are the same in Fig. 3.3(c) and 3.4(c). Thin solid line shows the distribution of the diabatic limit, which corresponds the infinite slew rate. In this situation, $\alpha^{(i)} = \beta^{(i)} = \gamma^{(i)} = 0$ ($i = 1, 2$) in Eq. (3.15) and the effect of the quantization axis rotation alone appears. On the other hand, for the bold solid and dotted curves, the slew rate is finite; 100V/(cm·μs) and 6V/(cm·μs), respectively. The effect of spin $\mathbf{I}_k$ rotation is small in the bold solid curve with slew rate=100V/(cm·μs), whereas it is large in the dotted curve with lower slew rate.

3.2   Time evolution in a ramped electric field

In Sec. 3.1 we have calculated the time evolution under the field rotation. After the zero crossing of F_z, adjacent manifolds begin to cross at $F = \frac{1}{3n^5}$ as F_z increases. The previous subsection's scheme cannot be applied to the evolution through avoided crossings, because the formulation does not include the ionic core effect of alkali atoms. Therefore, in this field region, we need to take another step. We have numerically solved the Schrödinger equation with Hamiltonian of Eq. (3.24) where the field is ramped by the slew rate S_z ($F_z(t) = S_z t$),

$$i\hbar \frac{d\psi}{dt} = H\psi. \tag{3.23}$$

$$H = \frac{1}{2}p^2 - \frac{1}{r} + S_z tz + V_d(r), \tag{3.24}$$

where ℓs coupling Λ, static field components F_x, F_y and the magnetic field terms are neglected because $F_z z \gg \Lambda, F_x x, F_y y$, and $\frac{\mathbf{B}\boldsymbol{\ell}}{2}$, as F_z grows after the field rotation.

Solving Eq. (3.23) for Rb Rydberg states have been performed with a computer program originally developed by Kishimoto [6]. In his previous work, the calculation is restricted to a small field about a few tens of mV/cm on the Stark map including several avoided crossings and the number of basis is not more than a few tens. We have extended the scheme to calculate the time evolution up to $F_z = 800$mV/cm ($n = 112$) by including all the states within $\Delta n = 5$. The total number of the states included becomes over one thousand in each magnetic quantum number. In the simulation, we need to calculate the evolution of only $|m_\ell| \leq 3$ states. It is because $|m_\ell| \geq 4$ states of Rb have negligible quantum defect. They propagate diabatically on the Stark map and ionize through the tunneling process like hydrogen.
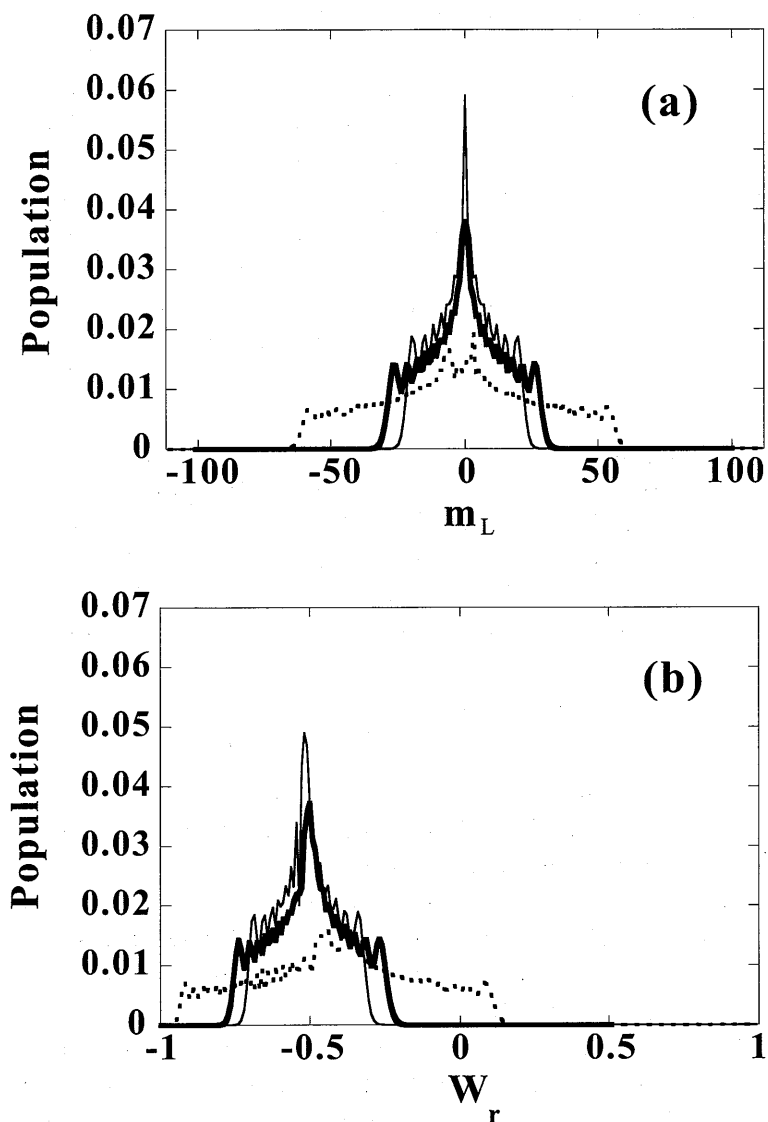
Figure 3.5: Calculated (a)m_ℓ and (b)W_r distribution after the field rotation with $F_x = 0$mV/cm, $F_y = 20$mV/cm and $\mathbf{B} = \mathbf{B_{geo}}$. Thin solid curve shows the diabatic limit corresponding to the case of the infinite slew rate. In this case, the spin $\mathbf{I}_k$ does not rotate and the redistribution of m_ℓ is due to only the rotation of the quantization axis. Bold solid and dotted curves represent distributions with slew rate $= 100$V/(cm·μs) and 6V/(cm·μs) respectively. The difference from the diabatic limit is due to the spin $\mathbf{I}_k$ rotation.

In Fig. 3.6, the time evolution of the populations of $n = 112$ Rb states is shown with $|m_\ell| = 0, 1, 2, 3$. The parameters are set to the same values adopted in the experiment of Sec. 5; the slew rate of the electric field is 5.9V/(cm·μs) and $W_r = -0.52$ with the quantization axis along the final F_z. In the figure, a dashed arrow shows the diabatic passage. States of $|m_\ell| = 0, 1, 2$ do not follow the diabatic path but rather go along with the adiabatic one, where energy of states does not change. The $|m_\ell| = 3$ states, however, still remain on the diabatic path at 0.8V/cm. This difference is reasonable because $|m_\ell| = 3$ states do not have $\ell = s, p, d$ components, which have much larger quantum defects than f state(see Table 2.2). Therefore, we concentrate only the evolution of $|m_\ell| = 3$ states in the following of this section.

In Fig. 3.7, populations on the diabatic paths for $|m_\ell| = 3$ states are shown with various slew rate, 1.5, 5.9 and 20.2V/(cm·μs). A population within $|\Delta n_1| \leq 3$, which corresponds to $|W_r| \leq 0.054$, is taken as a diabatic population. From the figure it is apparently seen that the faster slew rate becomes, the more diabatically the states propagate. The feature is indicated by the diabatic transition probability P in each avoided crossing,

$$P = \exp\left(-2\pi \frac{<V_d>}{\hbar \frac{d\Delta W}{dF} \cdot \frac{dF}{dt}}\right), \tag{3.25}$$

where $<V_d>$ is matrix element of $V_d(r)$ between the two states in the avoided crossing, ΔW is the difference of the energy between the two states and $\frac{dF}{dt}$ is a slew rate of a applied electric field.

Lines in Fig. 3.7 are the best fits of calculated points to the linear function. Extrapolating them up to the tunneling ionization threshold gives the fraction of the tunneling ionization process, which is shown in Table 3.1 with some parameters. From the table, we plot the n dependence of the tunneling fraction of $|m_\ell| = 3$ states in Fig. 3.8. The tunneling fraction increases as n grows. This feature comes from the decrease of $V_d(r)$ with increasing n as shown in Eq. (2.17), which increases the diabatic transition probability P in Eq. (3.25).

4   Experimental setup and procedure

In the present section, experimental setup and procedure are described. First, we show the overall setup of this experiment in Fig. 4.1. In the experiment, [85]Rb is used. A thermal atomic beam of Rb is introduced to the region surrounded by two ionization electrodes and two additional electrodes. The atoms are excited to the Rydberg states by a two-step excitation and
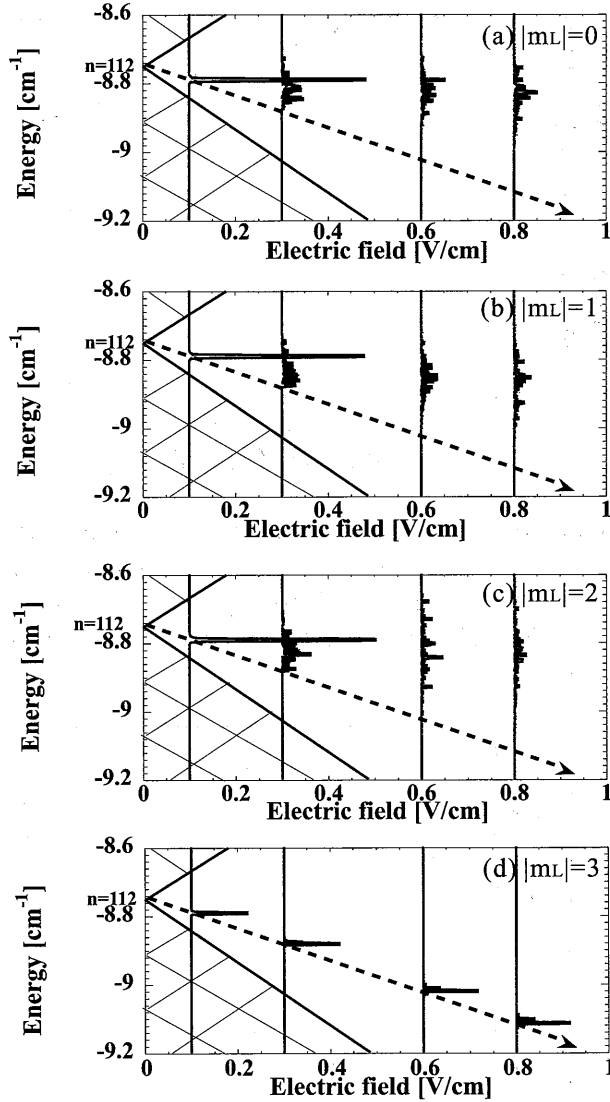
Figure 3.6: Time evolution of the population of the states with $n = 112$ under the ramped electric field; (a)$|m_\ell| = 0$, (b)$|m_\ell| = 1$, (c)$|m_\ell| = 2$ and (d)$|m_\ell| = 3$. Initial W_r is -0.52 and the initial $F_z = 5\text{mV/cm}$. The slew rate of the ramped electric field is $5.9\text{V/(cm·}\mu\text{s)}$. Dashed arrows show the diabatic paths. In (d), the drawing scale of the population is reduced to 20% from those of (a), (b) and (c) for clarity.
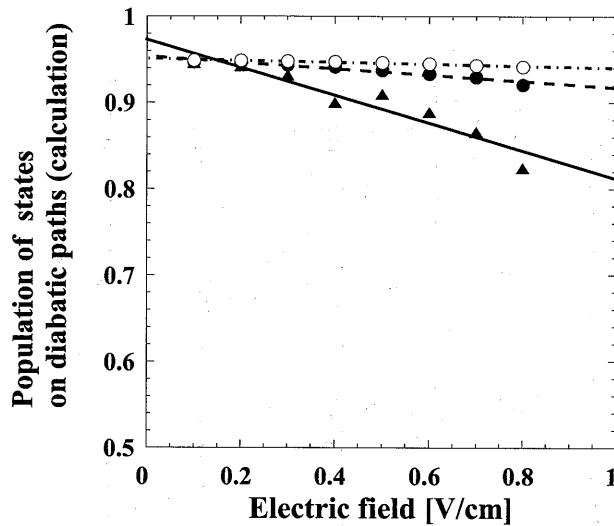
Figure 3.7: Calculated values of the population on the diabatic paths(broken arrow in Fig. 3.6) with slew rate = 1.5V/(cm·μs) (solid triangle), 5.9V/(cm·μs)(closed circle) and 20.2V/(cm·μs)(open circle). The principal quantum number n is 112 and initial W_r is -0.52. Lines represent best fits to the linear function.
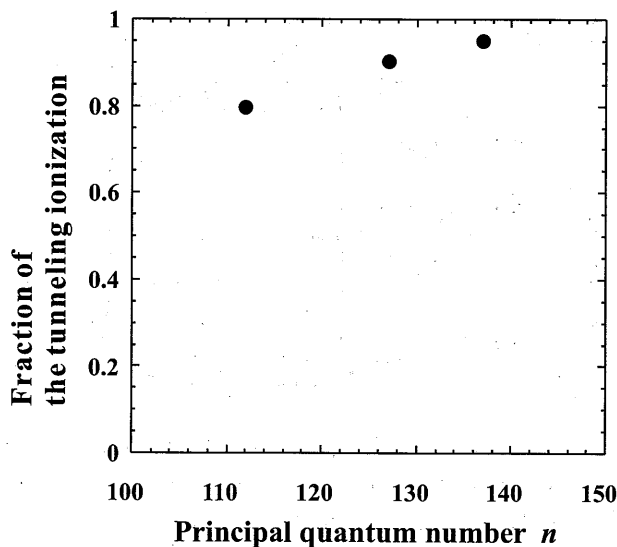

Figure 3.8: Principal quantum number n dependence of the tunneling ionization fraction of the state with $|m_\ell| = 3$. The slew rate of the ramped electric field is 5.9V/(cm·μs) and $W_r = -0.52$.

Table 3.1: Tunneling process fraction of $|m_\ell| = 3$

n	Slew rate [V/(cm·μ s)]	$W_r (= Z_1 - Z_2)$	Tunneling process ratio in $|m_\ell| = 3$
112	5.9	-0.30	0.76
112	1.5	-0.52	0.28
112	5.9	-0.52	0.80
112	20.2	-0.52	0.90
127	5.9	-0.52	0.90
137	5.9	-0.52	0.95

ionized by a pulsed electric field. Ionized electrons are collected by an electron multiplier and signals are recorded as time difference from the start of the ionization pulse. In the following of this section, dividing into four parts, the setup is explained by; an atomic beam setup, a laser excitation part, a field ionization setup and a detector and circuits. The experimental procedure is described at the end of this section.

4.1 Atomic beam

A glass cell containing ^{85}Rb is installed inside a beam oven in a vacuum chamber. The beam oven is heated by a heater, which is rolled over the oven. The aperture of the oven is 5mm, and it is placed 880mm away from the ionization electrodes. During the experiment the temperature of the beam oven was controlled and monitored to get the sufficient amount of Rydberg ionization signals. It is usually kept around $110°C$.

When Rb atoms are absorbed by the electrode or other devices in the vacuum chamber, it can be the cause of stray field. To prevent that, three cold traps cooled by liquid nitrogen are placed between the beam oven and the ionization electrodes. The traps have a hole for beam path. An aperture of 2mm diameter in a copper plate placed 15cm upstream from the electrodes restricts the beam spread to the size of 3.4mm diameter at the ionization electrodes.

4.2 Laser setup

Rydberg atoms are prepared by a two-step excitation as shown by Fig. 4.2. Firstly, a diode laser(Sharp GH0780MA2C) excites the atoms in the beam from the ground state($5s_{1/2}$) to the $5p_{3/2}$ excited state. Secondly, a ring dye laser(Coherent 899-29) excites the atoms in the $5p_{3/2}$ state to the final
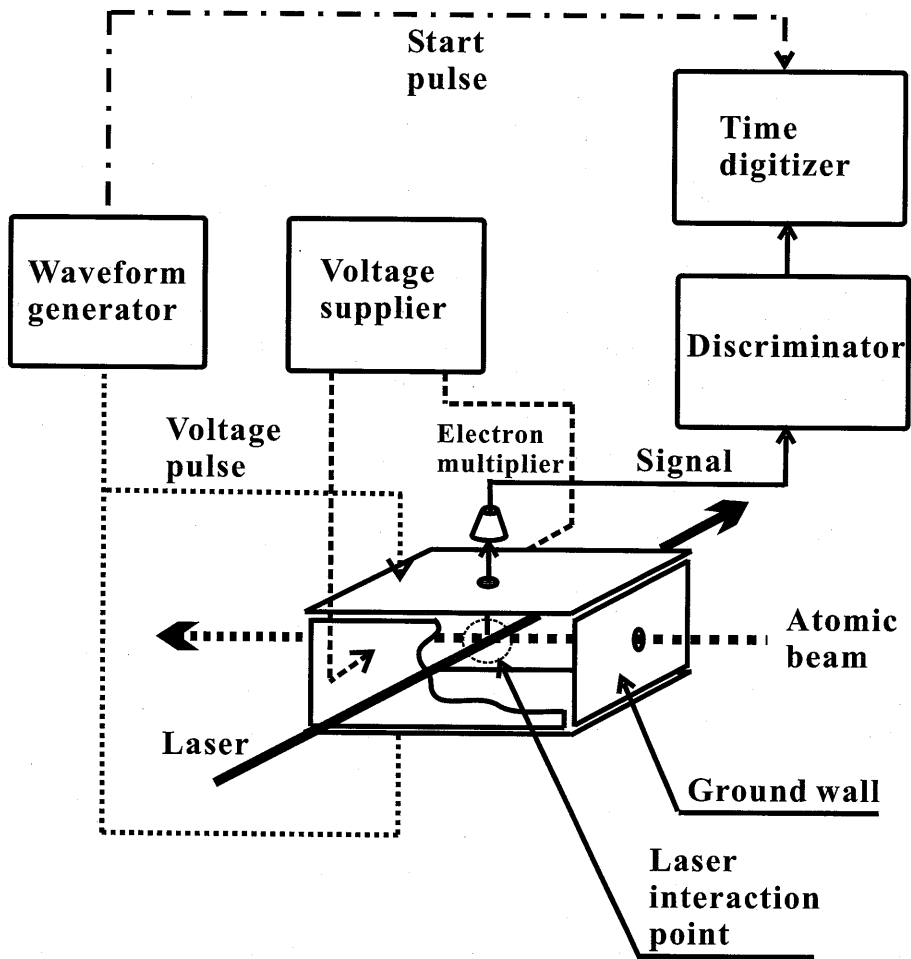
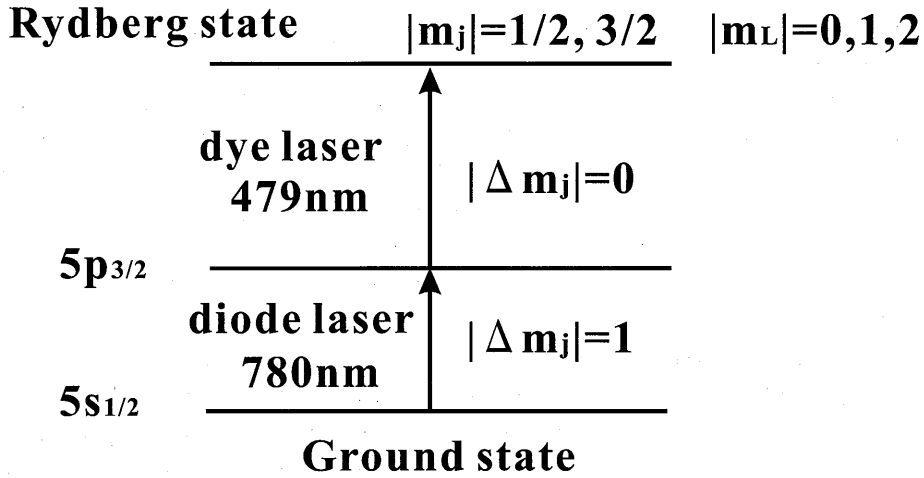Figure 4.1: Schematic view of the experimental setup.

Rydberg state $|\mathbf{m_j}|=1/2,\ 3/2$ $|\mathbf{m_L}|=0,1,2$

dye laser
479nm $|\Delta\, \mathbf{m_j}|=0$

5p$_{3/2}$ ————————————

diode laser
780nm $|\Delta\, \mathbf{m_j}|=1$

5s$_{1/2}$ ————————————

Ground state

Figure 4.2: Two-step laser excitation diagram for ^{85}Rb. The magnetic quantum number of the states is also shown. The quantization axis is taken along the ionization field direction in the experiment.

Rydberg states. The wavelength of the diode laser is 780nm and its power is 30mW. The wavelength is controlled by the current and the temperature of the diode. To keep the wavelength on the transition frequency between $5s_{1/2}$ and $5p_{3/2}$, the fluorescence signals from the deexcitation of the $5p_{3/2}$ state were measured with a separate atomic beam system and used to control the wavelength so that the amount of fluorescence becomes maximum.

The dye laser is pumped by a Kr ion laser(Spectra Physics SP2007). The wavelength is 479.27nm when a $n = 110$ state of Rb is excited. Its output power used in the experiment is about 80mW. To check the absolute wavelength, an absorption spectrum of tellurium molecules was also measured. The small amount of the dye laser light splitted by a slide glass is transmitted through a Te cell in a vacuum chamber. The power of the laser through the Te cell was measured with a photo diode.

In the experiment, the polarization of the diode and the dye laser is perpendicular and parallel to the ionization field, respectively. Therefore, $|m_J| = 1/2$ or $3/2$ states are allowed as a final Rydberg state by the selection rule as shown in Fig. 4.2. The state has components of $|m_\ell| = 0, 1, 2$.

4.3   Field ionization

Rb atomic beam is introduced to the region surrounded by the six Cu plates. The excitation and ionization of the Rydberg atoms are done inside

the region. In the six plates, voltage can be applied to the four of them, and the rest of them are electrically connected to the ground. The top and bottom electrodes are for pulsed electric field to ionize Rydberg atoms. The size of the ionization electrode is 210mm×210mm. There is a 5mm diameter hole in the top electrode through which ionized electrons are collected by the electron multiplier. The two side-electrodes are for generating static field perpendicular to the ionization field. The condition of the rotating field is changed by varying the voltage of the electrodes. The size of side electrodes is 210mm×60mm.

The pulsed electric voltage is produced by a waveform generator(Sony Tektronix AWG420). A typical waveform is shown in Fig. 4.4. After amplification, it is applied to the ionization electrodes. The field rises from 0V/cm to 6V/cm in $0.25 - 4\mu s$ in the experiment. The precise determination of the slew rate of the field was done by measuring the waveform with a digital oscilloscope.

4.4   Data acquisition

Ionized electrons are collected by a channel electron multiplier. Output signals of the multiplier are amplified by a charge sensitive pre-amplifier and two main amplifiers. After the amplification, the pulse height becomes several hundreds of mV and the FWHM of the pulse is about 30ns. The signals are then fed to a discriminator and counted by a multiple-event time digitizer P7886(Fast Comtec). Its time resolution is 500ps. It records the interval between a start signal of the pulsed electric field generated from the waveform generator and the signal from the discriminator.

To transform the timing information to the field strength information at which the ionization has occurred, the elapsed time from the ionization to arriving at the time digitizer should be known. We obtained this time information by measuring ionization spectra with several slew rates: Rydberg atoms are ionized at the same field strength, but the arrival time changes with the slew rate. As displayed in Fig. 4.3, the extrapolation of the ionization peak channel on the time digitizer to zero rise time(infinite slew rate) shows the elapsed time of the signal. Then we can get an ionization spectrum, which tells ionization electric field as shown in Fig. 4.4.

4.5   Experimental procedure

When the frequency of the dye laser is swept, there are several resonant peaks as shown in Fig. 4.5. By applying several tens of mV/cm in the region of excitation and ionization, the manifold of states can be excited as
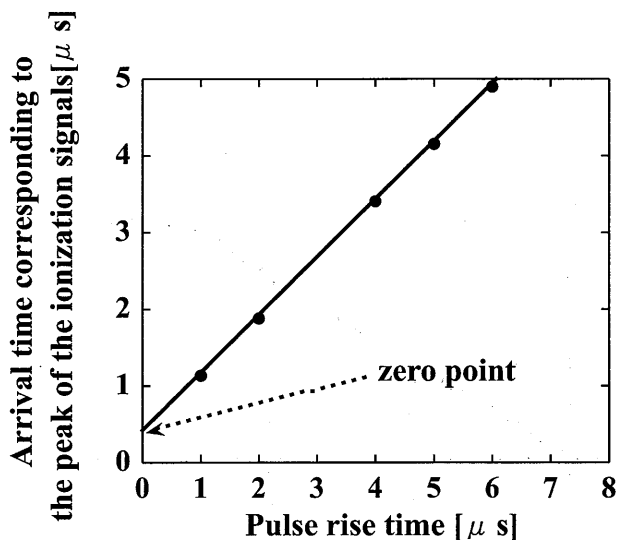
Figure 4.3: Arrival time corresponding to the peak of the ionization signals measured with the time digitizer is plotted with rise time of the pulsed electric field. The data were measured to obtain the zero point channel.

shown in the upper part of Fig. 4.5. While taking the ionization spectra, the laser frequency is locked to some states in the manifold. Typical ionization spectrum is shown in the lower part of Fig. 4.4. Two prominent peaks are shown in the spectrum. The peak in lower field is from autoionization-like process, and that in higher field is from tunneling process. From the spectrum, we have obtained the fraction of tunneling process in the all signals.

5   Experimental results and discussion

We have measured ionization spectra of Rydberg atoms of ^{85}Rb by changing the values of various parameters and obtained the fraction of the tunneling process and its dependence on them. The data are compared with the calculated results based on the scheme described in Sec. 3.

First, in Fig. 5.1 we show the relation between the coordinate system used in Sec. 3 and the experimental setup in Sec. 4 . The electrodes of A and A' in Fig. 5.1(c) generate a pulsed electric field for ionization, and those of B and B' make a static field for changing the condition of the field rotation. In addition to those applied fields, there is a stray field produced
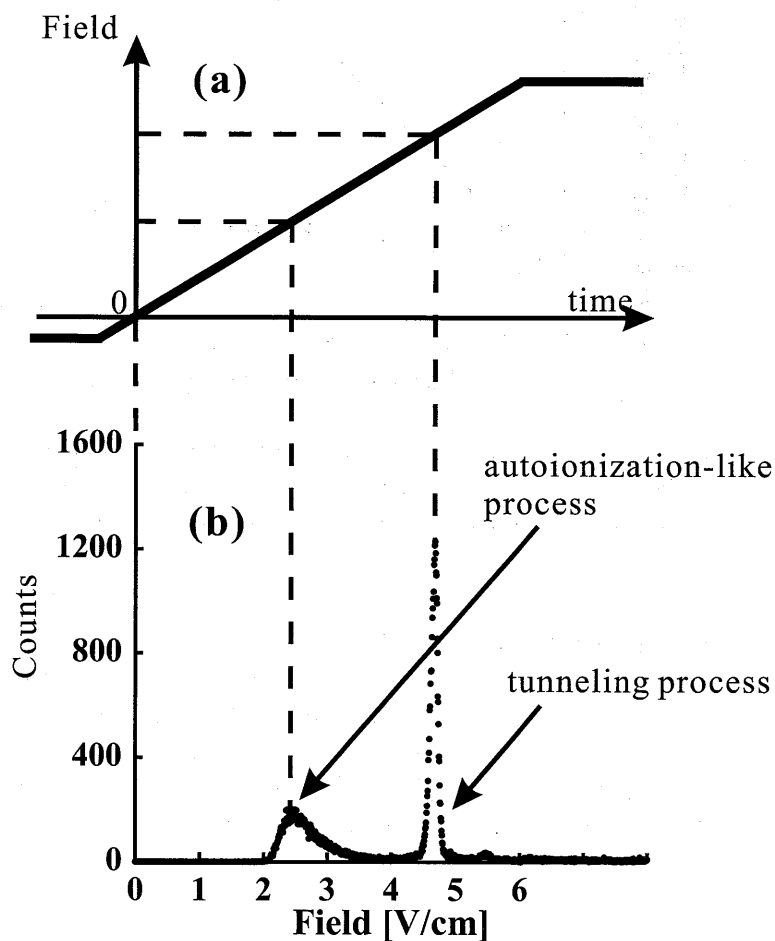
Figure 4.4: Schematic view of the applied pulsed field during the field ioniza-tion(upper part) and a resulting ionization spectrum(lower part). The timing signal is transformed to the field strength spectrum through the pulse profile. In the ionization spectrum, the lower threshold peak is from autoionization-like process and the higher one is from tunneling process.
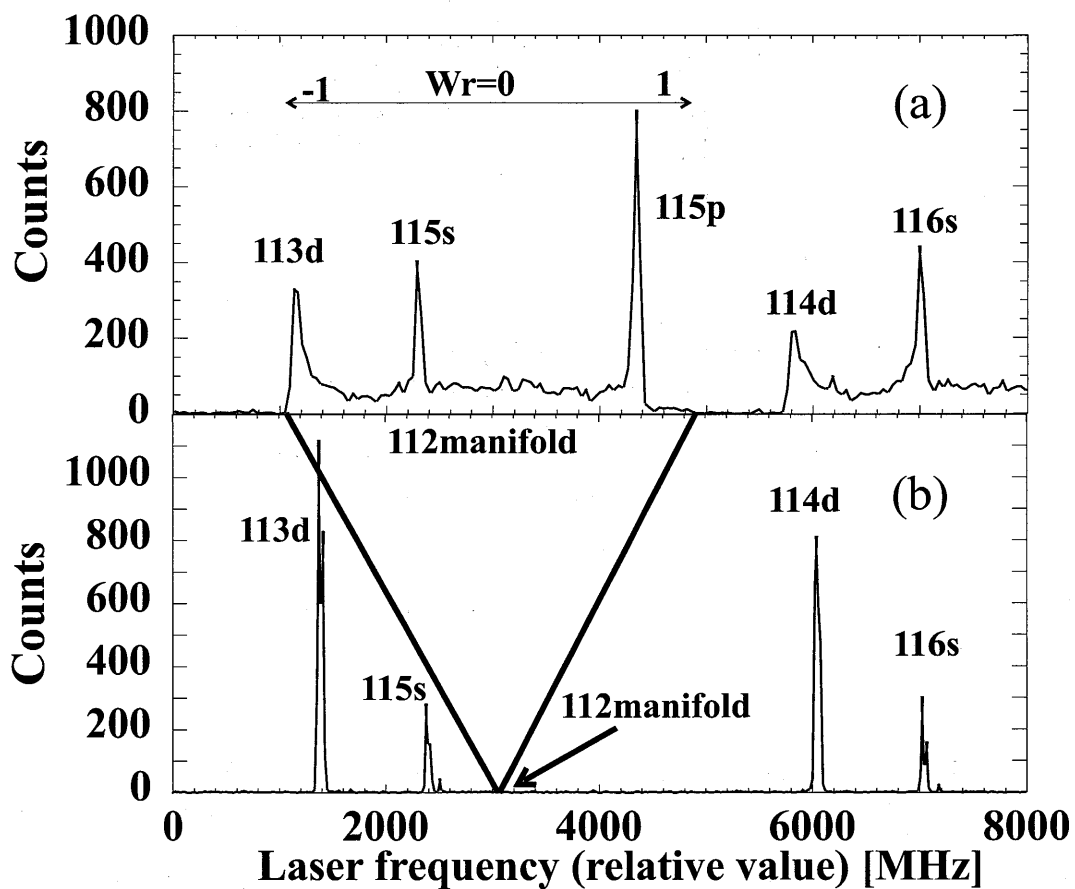
Figure 4.5: Excitation spectra of the $n = 112$ manifold states of ^{85}Rb with the applied electric field of (a) 80mV/cm, and (b) 0mV/cm.

(a)

South   West

East   North

(b)   **z**

F_x F_y y

x

F_z

F

F_x: **stray field**
F_y: **stray field+ field applied by BB'**
F_z: **stray field+ field applied by AA'**

(c)   atomic beam
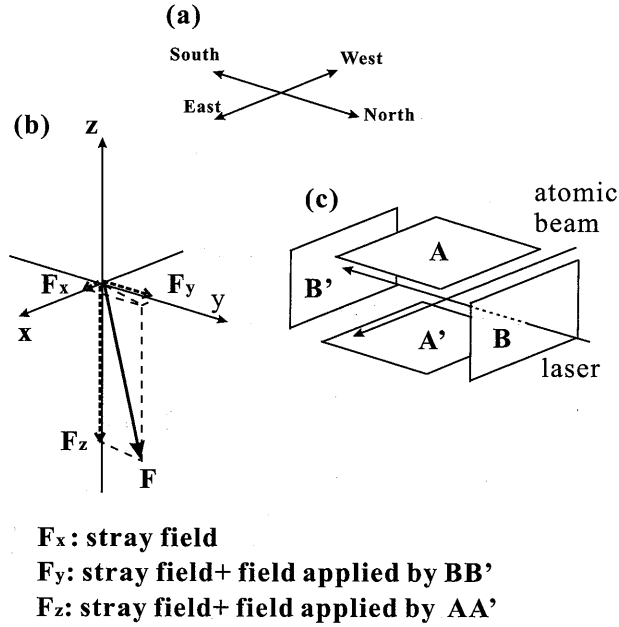
A

B'

A'   B

laser

Figure 5.1: Correspondence among (a) the geographical direction, (b) the coordinate system in the simulation and (c) the experimental setup.

by the surroundings such as surface contamination of electrodes. Here, we define $\mathbf{F}^{\mathrm{total}}$ as the field that Rydberg atoms feel and,

$$\mathbf{F}^{\mathrm{total}} = \mathbf{F}^{\mathrm{app}} + \mathbf{F}^{\mathrm{stray}}, \tag{5.1}$$

where $\mathbf{F}^{\mathrm{app}}$ is the applied field by the four electrodes, and $\mathbf{F}^{\mathrm{stray}}$ is the stray field. We also define $\mathbf{F}^{\mathrm{cal}}$ as the field in the calculation and we will use $\mathbf{F}$ as both $\mathbf{F}^{\mathrm{total}}$ and $\mathbf{F}^{\mathrm{cal}}$.

The stray field is reduced by the measures such as cleaning the electrode, taking a distance between Rydberg atoms' path and the surroundings. The stray field can be obtained by measuring Stark shifts of s and p states of Rydberg atoms [19] in the excitation spectrum. In the present experiment it was about 4.7mV/cm. In each component of $\mathbf{F}^{\mathrm{stray}}$, F_z^{stray} has little influence on the condition of the experiment, because the pulsed field varying through zero can cancel it. The value of F_y^{stray} was found to be about 1.3mV/cm from the measurement described in the next subsection. Therefore, only the value of F_x^{stray} remains unknown, which is less than 4.7mV/cm.

In other parameters of the following calculation, the initial value of $|m_\ell|$ was set to zero. In the experimental situation, however, $|m_\ell| = 1$ and 2

states can be populated by the laser excitation from $5p_{3/2}$. The effect of the difference is considered to be small after the large redistribution of m_ℓ such as shown in Fig. 3.3(c).

5.1   Effects of the rotating electric field

5.1.1   Change of the fraction of the tunneling ionization process with the transverse field F_y

First we have measured ionization spectra with changing F_y^{app}. The pulsed electric field F_z^{app} is ramped from 80mV/cm to about -6V/cm. It is the important result in this work to investigate the effect of the field rotation predicted in Sec. 3 experimentally. In Fig. 5.2, shown are the measured ionization spectra of the manifold states with $n = 112$. In the figure, F_y^{app} ranges from -21.7mV/cm to 21.5mV/cm. The fraction of the tunneling ionization peak, which appears at the higher ionization field in the two peaks, drastically changes with F_y^{app}.

The dependence of the tunneling ionization fraction on the value of F_y^{app} is shown in Fig. 5.3. The solid circles in the figure are the experimental data and the lines are the calculated values using the scheme described in Sec. 3. We concluded $F_y^{\mathrm{stray}} = 1.3$mV/cm because the tunneling ionization fraction have taken the lowest value when $F_y^{\mathrm{app}} = -1.3$mV/cm as shown in the figure. Therefore, the calculated values are plotted with the relation that $F_y^{\mathrm{cal}} = F_y^{\mathrm{app}} + 1.3$mV/cm. The initial value of W_r is 0.30 with the quantization axis along the z axis in Fig. 5.1.

In the experimental result, the tunneling ionization process increases with $|F_y^{\mathrm{app}}|$ and the fraction is over 0.9 with $|F_y^{\mathrm{app}}|$ of a few tens of mV/cm. The feature is also seen in the calculated data due to the $|m_\ell|$ redistribution over the wider range under the field rotation. Around $F_y^{\mathrm{cal}} = 0$, the calculated values sensitively change with the value of the stray electric field F_x^{cal} and the magnetic field, because they become dominant when F_z^{cal} is close to zero. On the other hand, when $|F_y|$ is large, the experimental result is in good agreement with all the calculation lines in the figure.

5.1.2   Redistribution of W_r in the ionization spectra

As mentioned in Sec.3.1.2, calculated W_r distributions can be compared with the measured tunneling ionization spectra, if we know the relation between W_r and ionization threshold of tunneling process. Here, we have used two methods to obtain the relation.

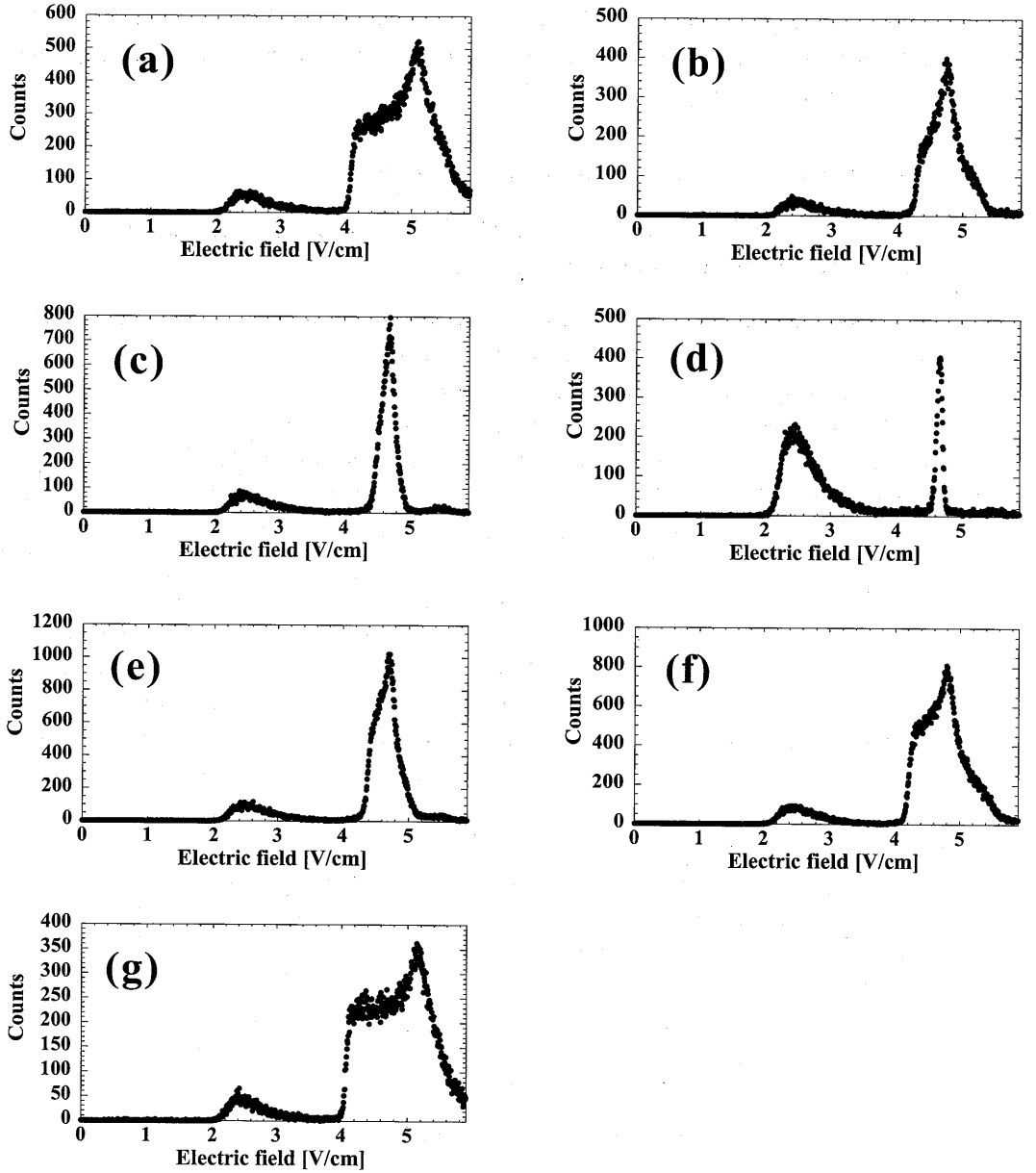In the first method, we have measured the ionization threshold of the

Figure 5.2: The measured ionization spectra for $n = 112$ with various traverse electric fields F_y^{app}; (a) $F_y^{app} = -21.7\text{mV/cm}$,(b) $F_y^{app} = -11.1\text{mV/cm}$, (c) $F_y^{app} = -5.3\text{mV/cm}$, (d) $F_y^{app} = -1.3\text{mV/cm}$, (e) $F_y^{app} = 5.6\text{mV/cm}$, (f) $F_y^{app} = 11.4\text{mV/cm}$ and (g) $F_y^{app} = 21.5\text{mV/cm}$. The initial value of W_r is 0.30 with a quantization axis along the z axis in Fig. 5.1. The slew rate of F_z^{app} is $5.9\text{V/(cm·}\mu\text{ s)}$
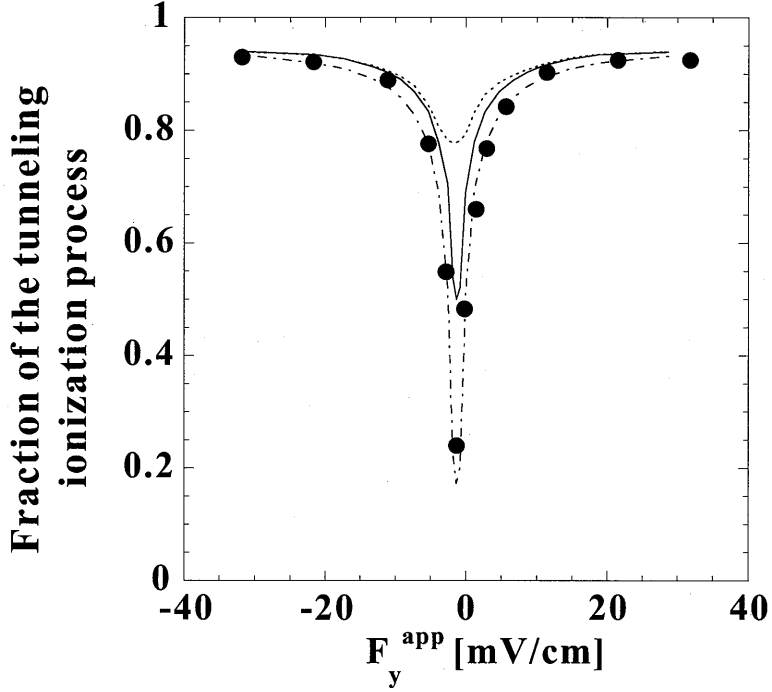
Figure 5.3: The F_y dependence of the tunneling process fraction for $n = 112$: Experimental data(solid circles) and calculated data(lines) are plotted. Three lines in the figure are calculated results with different values of F_x^{cal} and magnetic field; F_x^{cal}=0mV/cm and $\mathbf{B} = \mathbf{B}^{\mathrm{geo}}/2$ (dash-dotted-line), F_x^{cal}=0mV/cm and $\mathbf{B} = \mathbf{B}^{\mathrm{geo}}$ (solid line) and F_x^{cal}=5mV/cm and $\mathbf{B} = \mathbf{B}^{\mathrm{geo}}$ (doted line). The calculated lines are shifted by $\Delta F_y^{\mathrm{cal}} = -1.3$mV/cm for the dip of the calculated result to coincide with the experimental one. It is justified when we assume the existence of the stray field of 1.3mV/cm in the direction of the y axis. The initial value of W_r is 0.30 with a quantization axis along with z axis in Fig. 5.1. The slew rate of F_z is 5.9V/(cm·μ s)
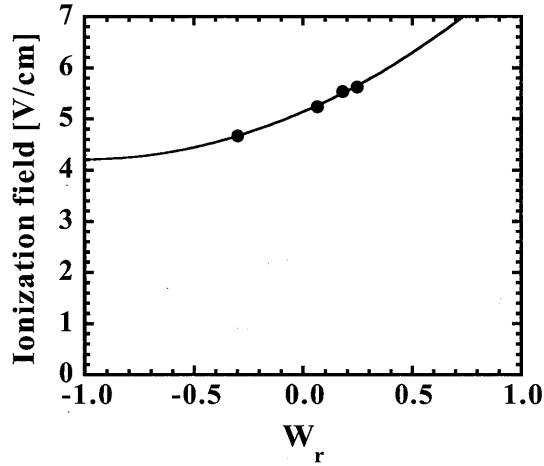
Figure 5.4: Tunneling ionization threshold values of $n = 112$ with F^{app} about zero at various positions W_r with the quantization axis along the final electric field direction. The solid circles are the experimental data and the solid curve is the best fit to the polynomials up to the second order terms with respect to the W_r. The fitting is aimed at obtaining the relation between W_r and ionization fields near the experimental data points.

tunneling process with $F^{\mathrm{app}} \simeq 0$ at several W_r, as shown in Fig. 5.4. Using the data we transform the measured ionization spectra to W_r distribution. In Fig. 5.5, W_r distribution with various F_y from measured and calculated data are shown. It is clear that the width of the peaks increases with F_y in both results.

In the above analysis, the difference of the ionization threshold with m_ℓ is not taken into account. If the range of m_ℓ distribution is small around zero, it does not affect the result in Fig.5.5. However, with large m_ℓ distribution we should include the effect in the transformation procedure. Therefore, as the second method, we have obtained the relation between W_r and the ionization threshold from the semi-empirical expression of ionization rate Γ for hydrogen developed by Damburg and Kolosov [20],

$$
\begin{aligned}
\Gamma \;=\;& \frac{(4R)^{2n_2+m_\ell+1}e^{-2R/3}}{n^3 n_2! (n_2 + m_\ell)!} \\
& \times \exp\left(-\frac{n^3 F}{4}\left(34n_2^2 + 34n_2 m_\ell + 46n_2 + 7m_\ell^2 + 23m_\ell + \frac{53}{3}\right)\right) (5.2)
\end{aligned}
$$

where $R = (-2E_0)^{3/2} F^{-1}$ and the energy E_0 is calculated up to the order
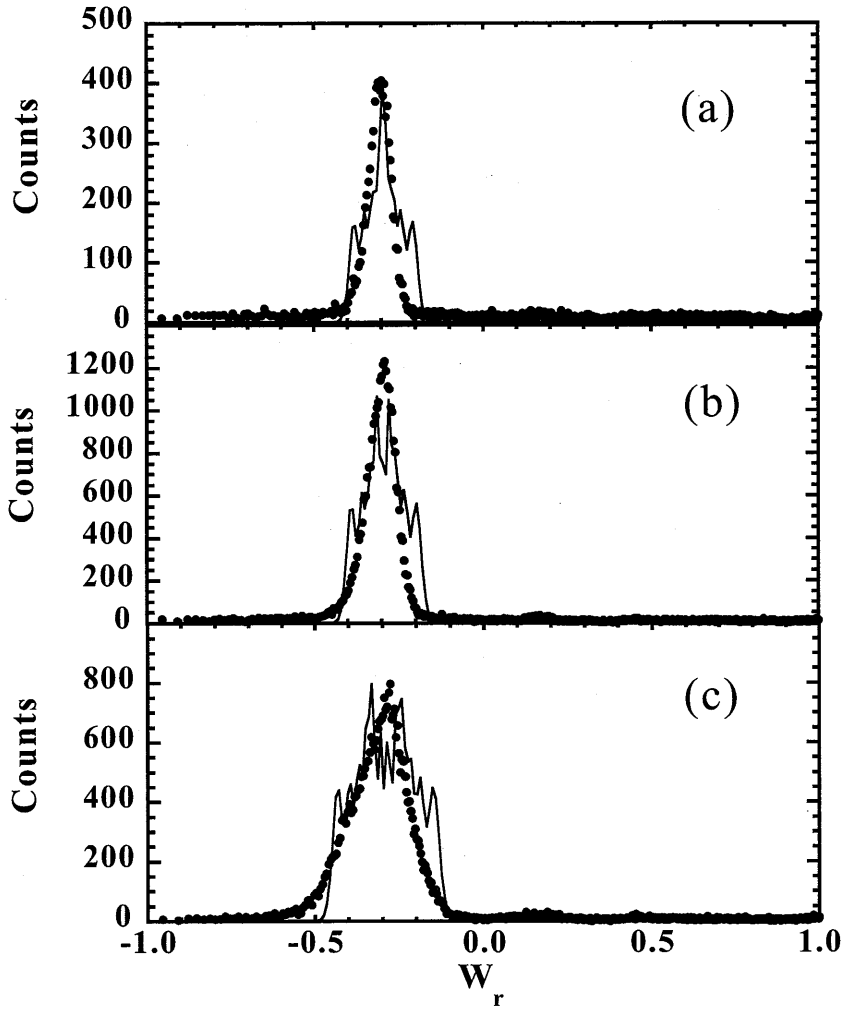
Figure 5.5: The experimental and calculated W_r distributions for $n = 112$ with various F_y^{total}; (a) $F_y^{\text{total}} = 0\text{mV/cm}$, (b) $F_y^{\text{total}} = -1.5\text{mV/cm}$ and (c) $F_y^{\text{total}} = -4\text{mV/cm}$. The value of W_r in the initial state is 0.3 and the slew rate of F_z is $5.9\text{V/(cm·}\mu\text{ s)}$. Solid circles are experimental data which are transformed from the ionization spectra using the relation between W_r and ionization threshold obtained in Fig. 5.4. Solid lines are calculated data with $F_x = 2\text{mV/cm}$ and $\mathbf{B} = \mathbf{B_{geo}}$.
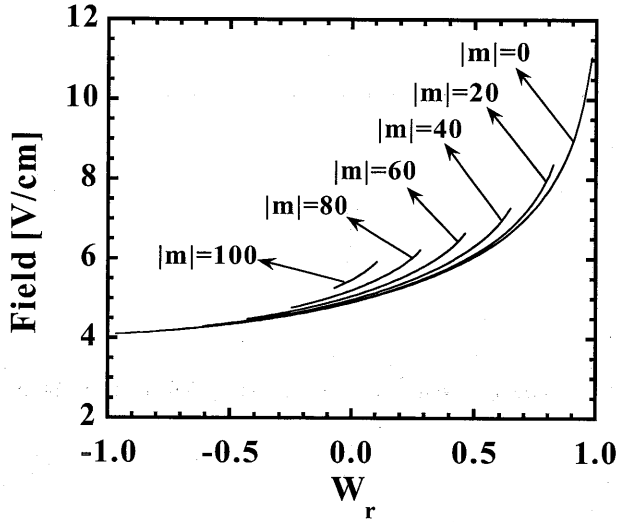
Figure 5.6: Ionization threshold of tunneling process of $n = 112$ state calculated with Eq. (5.2). The ionization field increases with $|m_\ell|$.

of F^4. We assumed the ionization threshold is equal to the electric field F at which $1/\Gamma = 0.1\mu s$. In Fig. 5.6, the tunneling ionization threshold from Eq. (5.2) of $n = 112$ state with various m_ℓ are displayed. We have applied this W_r-ionization threshold relation to the calculated W_r distribution and transformed to the ionization spectrum. Fig. 5.7 shows the experimental and theoretical results of $n=112$ states of ^{85}Rb with (a) $F_y = 0\text{mV/cm}$, (b) $F_y = 2.7\text{mV/cm}$, (c) $F_y = 6.9\text{mV/cm}$, (d) $F_y = 22.8\text{mV/cm}$ and (e) $F_y = 33.1\text{mV/cm}$. The absolute values of the peaks in the calculation(solid line in Fig. 5.7(a)) are found to be a little lower than the experimental results by 0.13V/cm, which is lower only less than 3% of the ionization field. One of the possible causes of the discrepancy may be due to that we have assumed ^{85}Rb states as the hydrogen states when using Eq. (5.2). Moreover, in our previous experiment [6] of Rb states with $n=120$, the calculated values have a tendency to be lower than the experimental results. Comparing the width of the peaks, the experimental and calculated results roughly coincide, which clearly shows the effect of the field rotation on the W_r distribution.

5.2   Slew rate and principal quantum number dependence

In Fig. 5.8, the fraction of the tunneling process with changing the slew rate of the ionization field is plotted. The experimental result shows slight
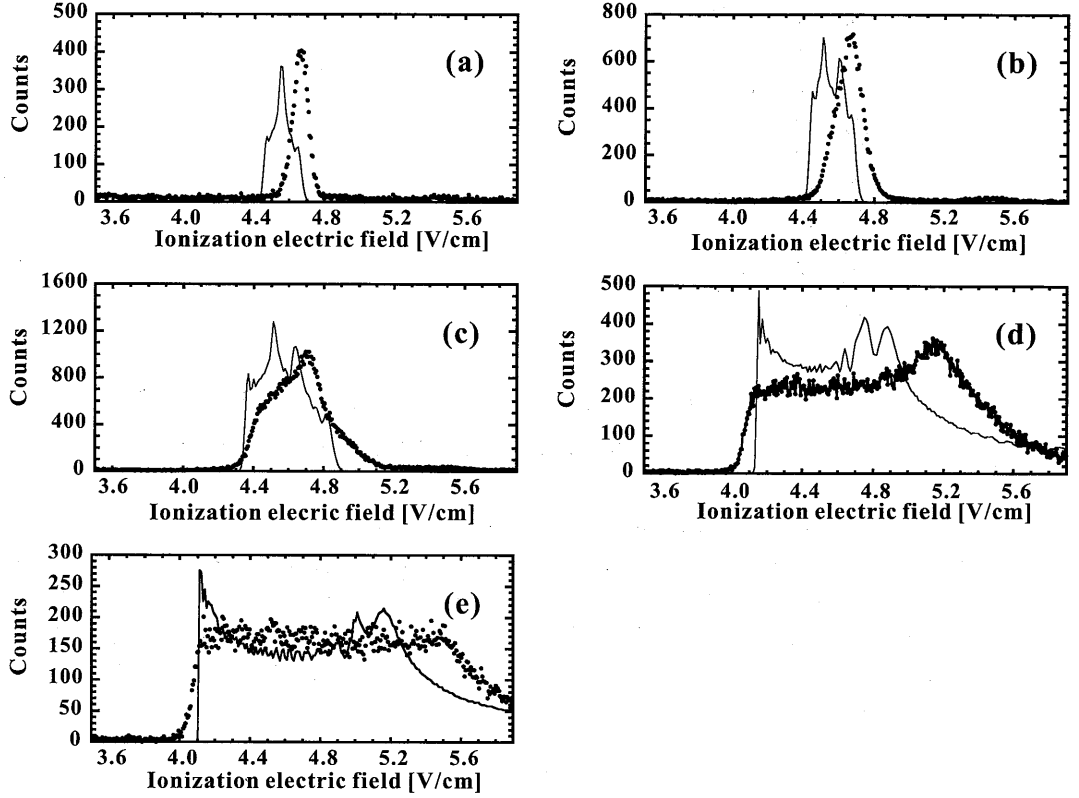
Figure 5.7: Experimental and calculated ionization spectra of the tunneling ionization process with various transverse fields F_y^{total}. Solid circles show the measured ionization field spectra of $n=112$ states of ^{85}Rb around the tunneling ionization threshold with various F_y^{total}; (a) $F_y^{total} = 0$ mV/cm, (b) $F_y^{total} = 2.7$mV/cm, (c) $F_y^{total} = 6.9$mV/cm, (d) $F_y^{total} = 22.8$mV/cm and (e) $F_y^{total} = 33.1$mV/cm assuming $F_y^{total} = F_y^{app}+1.3$mV/cm. Calculated results with the same F_y^{cal}, $\mathbf{B}^{geo}$ and $F_x^{cal} = 2$mV/cm are also shown by solid lines. They are transformed from W_r distribution using Eq. (5.2), in which the effect of the ionization field difference with m_ℓ is taken into account. The initial value of W_r is 0.52 with a quantization axis along the direction of the initial electric field. The slew rate of F_z^{app} and F_z^{cal} is 5.9V/(cm·μ s).
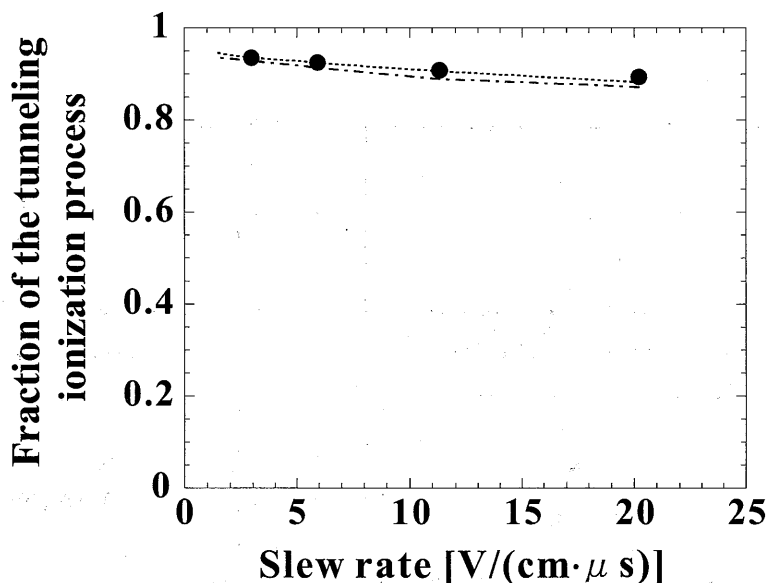
Figure 5.8: Slew rate dependence of the tunneling-process fraction of n=112 states of ^{85}Rb: Solid circles show the experimental results. Two lines are the calculated results with F_x^{cal}=0mV/cm and $\mathbf{B} = \mathbf{B}^{\mathrm{geo}}/2$ (dash-dotted line), and F_x^{cal}=5mV/cm and $\mathbf{B} = \mathbf{B}^{\mathrm{geo}}$ (dotted line), respectively. The initial value of W_r is 0.52 with a quantization axis along the direction of the initial electric field.

decrease with increasing slew rate, which is in good agreement with the calculated values. The cause of the decrease of the fraction is that the fast slew rate in the field rotation keeps the state to remain in the initial low-m_ℓ states, which ionize through the autoionization-like process.

The effect of increasing principal quantum number on the fraction was also measured, which is shown in Fig. 5.9. The experimental result shows almost flat distribution with increasing n. The calculated value shows slight decrease with increasing n. However, with larger F_x^{cal}, the calculated result is more approaching to the experimental value. Like the case of the slew rate dependence, the effect of the increasing diabatic transition probability P at avoided crossings, which makes the tunneling fraction larger shown in Fig. 3.8, has not been observed, because that of changing the m_ℓ distribution is dominant in this situation.
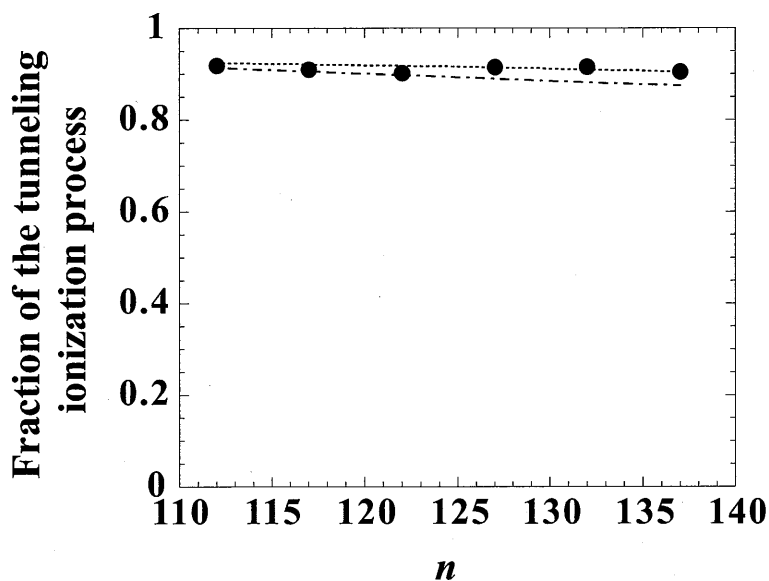
Figure 5.9: Principal quantum number n dependence of the tunneling-process fraction: Solid circles show the experimental results. Two lines show calculated results with $F_x^{\text{cal}}=0\text{mV/cm}$ and $\mathbf{B} = \mathbf{B}^{\text{geo}}/2$ (dash-dotted-line), and $F_x^{\text{cal}}=5\text{mV/cm}$ and $\mathbf{B} = \mathbf{B}^{\text{geo}}$ (dotted line), respectively. The initial value of W_r is 0.52 with a quantization axis along the direction of the initial electric field. The slew rate of F_z is $5.9\text{V/(cm·}\mu\text{ s)}$

5.3   Possible further improvement of the theoretical simulation

Although we have made several assumptions and approximations in the calculation, the results are generally in good agreement with experimental ones. Here, we discuss the further improvement of calculation.

In the present work we have adopted an approximation to neglect the quantum defects of ^{85}Rb and spin-orbit coupling in the calculation of the m_ℓ redistribution. More precise calculation of ^{85}Rb can be achieved by extending the treatment described in Sec.3.2 by replacing the Hamiltonian of Eq. (3.24) by

$$H = \frac{1}{2}p^2 - \frac{1}{r} + \mathbf{F}(t)\mathbf{r} + \frac{1}{2}\mathbf{B}(t)\boldsymbol{\ell} + \Lambda + V_d(r), \qquad (5.3)$$

where $\mathbf{F}$ is the electric field vector, $\mathbf{r}$ is a position vector of the electron, $\boldsymbol{\ell}$ is the angular momentum, Λ is the ℓs-coupling term and $V_d(r)$ is the quantum defect term. This scheme is applied to the dominant pulsed field

regime without approximation. However, the number of involved states with n about 112 becomes tremendously large because all the m_ℓ states have to be taken into account, which would be the practical difficulty of this method.

5.4　Application to selective field ionization

As described in Sec. 1, one of the aims of the present work is to enhance the tunneling ionization process by using the field rotation. The enhancement can improve the efficiency of the SFI method for highly excited Rydberg states.

First, we briefly describe the SFI method. In the work of Tada *et al.* [4], a SFI method for the 111*s* and 111*p* states of Rb was described. In a low electric field, *s* and *p* states are separated in energy from the manifold because of their large quantum defect. As the field increases they cross into the manifold as shown in Fig. 5.10(a). At the crossings, by applying a slowly growing field, adiabatic transitions from the *s* state to the lowest state and from the *p* state to the highest state in the manifold are realized. After the crossing, some fraction of the states proceeds as shown by arrows in Fig. 5.10(a) and ionized through the tunneling process. In the ionization spectra, the β peak from the *s*-state origin in Fig. 5.10(c) and the γ peak from the *p* state origin in Fig. 5.10(b) exhibit largely separated ionization thresholds. On the other hand the α peaks of the autoionization-like process have almost the same ionization field for both the *s* and *p* states as shown in Fig. 5.10(b) and (c).

We now return to the results of the present experiment. In Fig. 5.11, shown are the ionization spectra of $n = 112$ Rydberg states with(Fig. 5.11(b)) and without(Fig. 5.11(a)) transverse field F_y. The tunneling fraction abruptly increases from 20% in Fig. 5.11(a) to 90% in Fig. 5.11(b). It is noted here that the 20% fraction of the tunneling ionization in Fig. 5.11(a) may also come from the effect of stray field of perpendicular direction. If the stray field is smaller the difference of the tunneling ionization fraction between the two methods will be more magnified.

6　Conclusion

We have measured the ionization spectra of highly excited ^{85}Rb Rydberg states under the rotating electric field. The effects of the field rotation have been observed as the drastic increase of the fraction of the tunneling ionization and the broadening of the tunneling ionization peak. By calculating the time evolution of the Rydberg states, it has been revealed that these
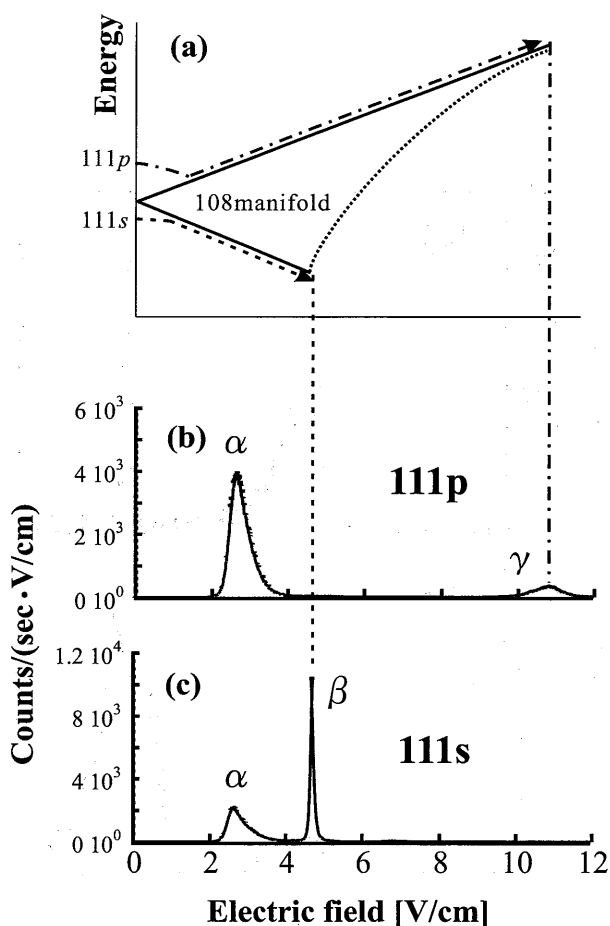
Figure 5.10: Schematic illustration of a method for the sensitive selective field ionization [4]: (a); the s(dashed arrow) and p states (dash-dotted-arrow) are manipulated to go though the Stark map along the lines shown in (a). It is noted that the crossing points of the s and p states in the Stark map in (a) are exaggerated. In (b) and (c); ionization spectra of $111p$ and $111s$ using above method. The data are cited from [4]. In the ionization spectra, α peaks are the ionization peaks through the autoionization-like process and β and γ peaks are those through the tunneling ionization process of $111s$ and $111p$, respectively.
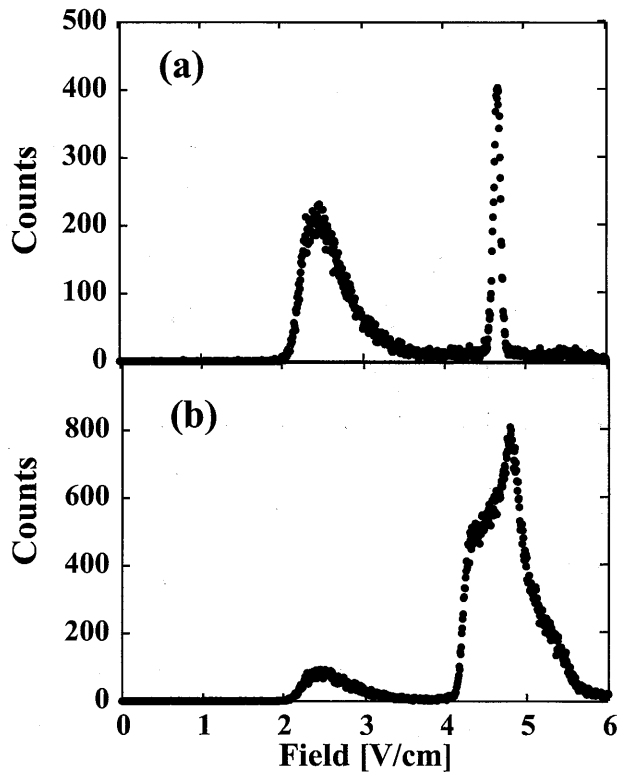
Figure 5.11: Ionization spectra of Rb states for $n = 112$ with (a)$F_y^{\text{total}} = $ 0mV/cm and (b)$F_y^{\text{total}} = 12.7$mV/cm. The initial value of W_r is 0.30, with a quantization axis along the initial electric field. The slew rate of F_z^{app} is 5.9V/(cm·μ s).

effects are due to the magnetic quantum number m_ℓ and the position in the manifold W_r redistribution under the rotating electric field.

In the present experiment, we excited a Rydberg state in the manifold of $112 \leq n \leq 137$ under the static electric field. Then the pulsed field was reversed from several tens of mV/cm through zero field and increased to about 6 V/cm to ionize the state. In addition to that ionization field, we applied a small amount of the static electric field perpendicular to the field for ionization. The tunneling fraction has abruptly increased from 0.2 to 0.9 by applying the perpendicular field of 20mV/cm, which clearly has shown the effect of the perpendicular field and demonstrated the magnetic-substate redistribution under the rotating field. The slew rate and n dependence of the fraction has also been measured. The fraction is almost the same with n ranging from 112 to 137 and decreases slightly with increasing slew rate of the pulsed electric field in the range from 1.5 to 20.2V/(cm·μs).

The present theoretical study of the behavior of the Rydberg states under the field rotation is mainly aimed to calculate the fraction of the tunneling process of ionization, which should be compared with the experimental results. It consists of two parts: Firstly the time evolution during the field rotation has been calculated and the results have shown that the field rotation causes the initial low-$|m_\ell|$ states are depopulated by the redistribution of m_ℓ states over very wide range. Secondly, to obtain the fraction of the tunneling process of each m_ℓ state, we have performed the calculation of the time evolution of the states of Rb on the Stark map. The parameters are set to those reproducing the experiment at conditions; n over the range of 112 to 137 with slew rate varying from 0.7 to 20V/(cm·μs). As a result, the state of $|m_\ell|$=0,1 and 2 and a small amount of the state of $|m_\ell|$=3 propagate on Stark map adiabatically and are ionized through the autoionization-like process. The other high $|m_\ell|$ states are ionized through the tunneling process.

From the simulation results, the increase of the tunneling process fraction observed in the experiment is understood by the scheme that the field rotation causes the decrease of states with $|m_\ell|$ =0,1 and 2, which are ionized through the autoionization-like process. The W_r distribution of the simulation results are also in good agreement with the measured ionization spectra.

From the viewpoint of application of Rydberg atoms to such as the high-efficient single-microwave-photon detection, the increase of the tunneling process fraction has vital importance to improve the efficiency of the selective field ionization of s and p states with high-n, because the only tunneling ionization peaks are distinguishable in such high-n states whose interval is in GHz range. In the present work, the fraction of tunneling ionization increases over 0.9 by the rotating electric field.

In the present experiment, the increase of the tunneling ionization fraction was found to be rather insensitive to experimental parameters such as a principal quantum number and a slew rate of the ionization field pulse. This is due to the fact that the $|m_\ell|$-changing effect arising from the electric field rotation is still in the intermediate stage between the adiabatic or diabatic time evolution in the present experiment. In the range of the parameters studied here, the efficiency of the photon detection with use of the tunneling ionization process is thus kept to high values.

Acknowledgments

The author would like to express my sincere gratitude to Prof. Ken'ichi Imai, who is a head of Experimental Nuclear and Hadronic Physics Laboratory, for his kind support and encouragement for the present work. The author would like to appreciate Prof. Katsuji Yamamoto for his advice and encouragement.

The author is thankful for kind help and encouragement from Dr. Yasuhiro Kishimoto, Dr. Tomohito Haseyama, Mr. Chikara Ooishi, Mr. Tomoya Saida and Mr. Terunao Nakura.

The author would like to thank Dr. Masaru Tada, Mr. Kentaro Kominato and Mr. Masahiro Shibata, for their help in the experiment and various discussions.

The author sincerely thanks Dr. Haruhiko Funahashi for his invaluable advice, discussions and kind supports in the present study.

The author is deeply grateful to my academic adviser, Prof. Seishi Matsuki. He has supported me in all the aspects of this work and his guidance is essential for it.

This research was partly supported by the Japan Society for the Promotion of Science.

References

[1] S. Matsuki, I. Ogawa and K. Yamamoto, *Phys. Lett. B* **336** (1994) 573.

I. Ogawa, S. Matsuki and K. Yamamoto, *Phys. Rev. D* **53** (1996) R1740.

K. Yamamoto and S. Matsuki, *Nucl. Phys. B Proc. Suppl.* **72** (1999) 132.

M. Tada, Y. Kishimoto, K. Kominato, M. Shibata, H. Funahashi, K. Yamamoto, A. Masaike and S. Matsuki, *Nucl. Phys. B Proc. Suppl.* **72** (1999) 164.

[2] T. F. Gallagher, *Rydberg Atoms* (Cambridge University Press, Cambridge, England, 1994) and references cited therein.

[3] Y. Kishimoto, M. Tada, K. Kominato, M. Shibata, S. Yamada, T. Haseyama, I. Ogawa, H. Funahashi, K. Yamamoto and S. Matsuki, *Phys. Lett. A* **303** (2002) 279.

[4] M. Tada, Y. Kishimoto, M. Shibata, K. Kominato, S. Yamada, T. Haseyama, I. Ogawa, H. Funahashi, K. Yamamoto and S. Matsuki, *Phys. Lett. A* **303** (2002) 285.

[5] A. K. Kazansky and V. N. Ostrovsky, *J. Phys. B* **29** (1996) L855.

[6] Y. Kishimoto, *Memoirs of the Faculty of Science, Kyoto University, Series of Physics, Astrophysics* (2001)

[7] M. Førre and J. P. Hansen, *Phys. Rev. A* **67** (2003) 053402.

[8] C. Higgs, M. A. Fineman, F. B. Dunning and R. F. Stebbings, *J. Phys. B* **15** (1982) L697.

[9] R. G. Rolfes, D. B. Smith and K. B. MacAdam, *J. Phys. B* **16** (1983) L533.

[10] M. Gross and J. Liang, *Phys. Rev. Lett.* **57** (1986) 3160.

[11] J. C. Day, T. Ehrenreich, S. B. Hansen, E. Horsdal-Pedersen, K. S. Mogensen and K. Taulbjerg, *Phys. Rev. Lett.* **72** (1994) 1612.

[12] K. S. Mogensen, J. C. Day, T. Ehrenreich, E. H. Pedersen, and K. Taulbjerg, *Phys. Rev. A* **51** (1995) 4038.

[13] L. Kristensen, E. Horsdal-Pedersen and P. Sørensen, *J. Phys. B* **31** (1998) 1049.

[14] R. Lutwak, J. Holley, P. P. Chang, S. Paine, D. Kleppner and T. Ducas, *Phys. Rev. A* **56** (1997) 1443.

[15] J. R. Rubbmark, M. M. Kash, M. G. Littman, and D. Kleppner, *Phys. Rev. A* **23** (1981) 3107.

[16] Yu. N. Demkov, B. S. Monozon and V. N. Ostrovskiĭ, *Zh. Eksp. Teor. Fiz.* **57** (1969) 1431 (Engl. transl. *Sov. Phys.-JETP* **30** (1969) 775).

[17] W. Pauli, *Z. Physik* **36** (1926) 336.

[18] L. D. Landau and E. M. Lifshitz, *Quantum Mechanics* (Oxford: Pergamon, 1977).

[19] T. Haseyama, K. Kominato, M. Shibata, S. Yamada, T. Saida, T. Nakura, Y. Kishimoto, M. Tada, I. Ogawa, H. Funahashi, K. Yamamoto and S. Matsuki, *Phys. Lett. A* **317** (2003) 450.

[20] R. J. Damburg and V. V. Kolosov, *J. Phys. B* **12** (1979) 2637